ACCSCIENCE PUBLISHING

Materials Science in Additive Manufacturing

ORIGINAL RESEARCH ARTICLE

Achieving a balanced duplex microstructure and corrosion resistance in UNS S32707 hyper-duplex stainless steel fabricated using GMAW-based wire arc additive manufacturing

Muppala Prardhan Yogya and Arivazhagan Natarajan*

School of Mechanical Engineering, Vellore Institute of Technology, Vellore, Tamil Nadu, India

Abstract

UNS S32707 Hyper-duplex stainless steels (HDSS) offer an attractive combination of high strength and corrosion resistance for demanding marine and offshore applications. A UNS S32707 HDSS wall was fabricated using gas metal arc welding (GMAW) combined with wire arc additive manufacturing (WAAM) for the subsea umbilical in marine engineering applications. The aim is to achieve a 50:50 ratio of austenite and ferrite phases and to suppress the formation of secondary phases; the balanced phase ratio provides a combination of mechanical properties and corrosion resistance. Microstructure evolution, mechanical behavior, and corrosion resistance of as-deposited UNS S32707 HDSS were comprehensively investigated. The electron backscatter diffraction analysis depicted a balanced duplex structure consisting of 52.1% ferrite, 47.4% austenite, and 0.5% sigma (σ) phase at the grain boundaries. The microstructure exhibited ferrite, intragranular austenite, Widmanstätten austenite, and grain-boundary austenite. Secondary phases, such as Cr_2N, secondary austenite (γ_2), and the chi (χ) phase, were not observed due to lower heat input and suitable inter-pass temperature. The tensile tests in three orientations (0°, 45°, 90°) relative to the build direction showed ultimate tensile strengths ranging from 927 MPa to 943 MPa, with elongations of 44% and an average hardness of 334 $HV_{0.5}$. Fractographic analysis revealed ductile failure, exhibiting finer and more uniform dimples. The corrosion studies conducted using a potentiodynamic polarization test in a 3.5 wt.% NaCl solution showed good corrosion resistance, with a low corrosion rate of 0.07877 mm/year. These findings establish controlled GMAW-based WAAM as a promising route for producing phase-balanced UNS S32707 HDSS for demanding marine applications.

Keywords: Hyper-duplex stainless steel (HDSS); Wire arc additive manufacturing; Gas metal arc welding; Electron backscatter diffraction analysis; Electrochemical corrosion behavior

***Corresponding author:**
Arivazhagan Natarajan
(narivazhagan@vit.ac.in)

Citation: Yogya MP, Natarajan A. Achieving a balanced duplex microstructure and corrosion resistance in UNS S32707 hyper-duplex stainless steel fabricated using GMAW-based wire arc additive manufacturing. *Mater Sci Add Manuf.* 2026;5(3):026280066. doi: 10.36922/MSAM026280066

Received: July 8, 2026

Revised: August 11, 2026

Accepted: August 17, 2026

Published online: September 17, 2026

Copyright: © 2026 Author(s). This is an Open-Access article distributed under the terms of the Creative Commons Attribution License, permitting distribution, and reproduction in any medium, provided the original work is properly cited.

Publisher's Note: AccScience Publishing remains neutral with regard to jurisdictional claims in published maps and institutional affiliations.

1. Introduction

The global market for duplex stainless steels (DSS) is valued at USD 5.83 billion in 2026 and is projected to grow at a compound annual growth rate of 6.31% by 2034.[1] Wire arc additive manufacturing (WAAM) is a directed energy deposition (DED) process, and

it is a type of welding that uses a filler wire as feedstock material and uses an electric arc to melt it, depositing layer by layer on the base plate using a pre-programmed multi-axis robotic arm that follows a pre-defined deposition tool path. WAAM offers the highest deposition rates among all other metal additive manufacturing techniques,[2] making it a cost-effective and viable method for fabricating medium- to large-scale metallic components with minimal material wastage.[3] WAAM can be performed using various arc welding techniques, such as gas tungsten arc welding,[4] plasma arc welding, gas metal arc welding (GMAW), and cold metal transfer.[5] Among all the variants, GMAW-based WAAM is a particularly suitable candidate for steel component fabrication, as it offers a high deposition rate (3–4 kg/h),[6] with improved tensile strength, toughness, and fatigue resistance.[7,8]

Hyper-duplex stainless steel (HDSS) is a superior category of DSS and contains a highly alloyed composition of Cr, Mo, C, Mn, Ni, Si, N, and Cu. The unique elemental composition of the alloy results in a dual-phase microstructure with approximately a 50:50 ratio of austenite and ferrite. The austenite phase provides toughness, and the ferrite phase contributes high strength. The pitting resistance equivalent number (PREN) is greater than 48, offering superior mechanical strength, wear resistance, and corrosion resistance in acidic chloride environments. The yield strength of HDSS is 20% greater than that of super duplex stainless steel (SDSS).[9-11] The combination of these properties makes HDSS particularly suitable for subsea umbilical systems in marine petrochemical applications that connect control stations to seabed wellheads, transmitting critical control signals and chemical supplies for subsea oil and gas operations.[12,13] Due to its high alloying-element content, secondary phases such as secondary austenite (γ_2), chi (χ), sigma (σ), and chromium nitride (Cr_2N) readily form at elevated temperatures. These phases affect the hardness and brittleness of the material, reducing its mechanical properties and corrosion resistance.[14] Therefore, the service temperature of the material is generally limited to below 90 °C. Furthermore, HDSS has been produced via casting,[10] powder injection molding (PIM),[15] and selective laser melting (SLM);[16] each of these methods has limitations: casting and PIM work on slow cooling rates, promoting secondary phase precipitation and diminished austenite content, while SLM produces finer microstructures confined to small-scale components with an imbalanced phase ratio of 59.5:40.5.[16] To overcome these limitations, it is necessary to develop a new manufacturing process. DED-based WAAM offers the advantage of producing large-scale, near-net-shape components with controllable thermal histories through inter-pass temperature management, making it a compelling candidate for HDSS fabrication.[17] Many studies have investigated the effect of WAAM on different grades of steel,[18-21] achieving enhanced mechanical properties and microstructural evolution.

A critical challenge in WAAM of duplex-family steels is controlling the formation of secondary phases, such as γ_2, χ, σ, and Cr_2N.[22] In WAAM, the upper layers experience progressively higher preheat temperatures from previously deposited material due to compounded cyclic thermal history (CCTH), resulting in complex microstructural gradients along the build height.[23-25] The literature shows that temperatures within the critical range (600 °C–1,000 °C) promote the generation of secondary phases.[26-29] At the optimal annealing temperature of 1,100 °C, HDSS promotes an equal percentage of ferrite and austenite.[14,30] In the present study, the objective is to achieve balanced phase fractions and suppress secondary phases directly through optimized WAAM process parameters, without requiring post-deposition heat treatment, thereby reducing manufacturing cost and lead time.

Wang *et al.*[31] investigated the microstructural changes of HDSS during solidification. Their results showed that a higher ferrite volume ratio could be achieved by increasing the cooling rate, a feature not possible with conventional casting. By optimizing WAAM process parameters and providing idle time between layers, where cooling occurs through air, it is possible to produce HDSS with improved mechanical properties and well-balanced phase compositions, and to achieve a faster cooling rate through air.[25] Numerous studies have been conducted on DSS and SDSS through different WAAM routes and have significantly achieved a balanced phase fraction of austenite and ferrite. This influences the microstructural and mechanical behavior.[32,33] However, to date, no study has reported GMAW-based WAAM of UNS S32707 HDSS, representing a critical gap in the literature. This necessitates studying the strength–ductility trade-off of HDSS developed through the GMAW-based WAAM process.

Industries are in demand for manufacturing critical components with HDSS through WAAM. Additionally, these applications require a balanced phase fraction of ferrite and austenite and to be free from secondary phases. Hence, this study investigates the effect of inter-pass temperature on the microstructure and tensile strength of HDSS produced using the GMAW-based WAAM technique. The relationship between process structure and properties and its effects on mechanical integrity was comprehensively investigated using optical microscopy, scanning electron microscopy (SEM)–energy-dispersive spectroscopy (EDS), and electron backscatter diffraction (EBSD)-driven

microstructure analysis. Corrosion behavior was evaluated using potentiodynamic polarization and electrochemical impedance spectroscopy (EIS) techniques.

2. Materials and methods

2.1. WAAM deposition and process parameter selection

A wall structure was developed using the GMAW-based WAAM process with UNS S32707 HDSS filler wire (1.2 mm diameter) deposited on an SS347 substrate. The deposition was carried out using an OTC Daihen FD-B6 six-axis robotic arm (OTC DAIHEN, Japan) equipped with an AF-4012 wire feeder, an FD-11 controller, and a DM 350 MIG/MAG power source (Figure 1). The robotic arm was pre-programmed to ensure consistent bead placement and precise geometry. Process parameters were optimized systematically using a bead-on-plate, trial-and-error, iterative technique. In these preliminary trials, the welding current, arc voltage, wire feed speed, and torch travel speed were varied to study their effects on bead shape, fusion quality, and inter-layer dilution. The dilution percentage was measured geometrically by evaluating the cross-sectional profiles of individual beads and calculating the ratio of the melted substrate area to the total cross-sectional area of each bead. An acceptable dilution level of 15%–20% was achieved, providing sufficient metallurgical bonding between successive layers without significant intermixing with the substrate material. The final optimized settings were as follows: torch travel speed was 200 mm/min, welding current was 120 A, and arc voltage was 11.11 V (Table 1). The shielding gas was supplied as industrial-grade pure argon with a constant flow rate of 14 L/min to prevent oxidation during deposition. The heat input (*HI*) was determined using **Equation 1**:

$$\mathrm{HI} = \frac{0.8 \times V \times I}{W \times 1000} \ (\mathrm{kJ/mm}) \qquad (1)$$

where V is the voltage (V), I is the current (A), and W is the arc running speed (mm/s), resulting in a heat input of 0.2601 kJ/mm. Each layer was deposited in one pass under ambient air-cooling conditions, and the inter-pass temperature was maintained at 110 °C–150 °C with a three-minute dwell time between successive layers for proper solidification. A total of 52 layers were deposited, giving a wall height of 118 mm and a thickness of 10 mm. The schematic representation of the WAAM deposition process is shown in Figure 2. Post-fabrication, the wall was separated from the base plate using electrical-discharge-machining wire-cutting (Figure 3a). The surface was then machined using a computer numerical control grinding machine (Pinnacle CNC 3X 8040, India) to achieve a smooth finish (Figure 3b). To verify weld defects and porosity in the deposited wall, non-destructive testing using X-ray radiography (YXLON SMART EVO 300P, Denmark) was performed in accordance with ASTM E1742/E1742M. The examination confirmed that the fabricated HDSS wall was free of defects, including porosity and cracking. The material composition of the WAAM-fabricated HDSS plate was determined using optical emission spectroscopy (OES; Q4 TASMAN, Bruker, Germany), and the measured elemental contents are reported in Table 2.

Table 1. Optimized process parameters of GMAW-based WAAM

Deposition parameters	Unit	Value
Current (I)	A	120
Voltage (V)	V	11.11
No. of depositing layers	–	52 layers
Shielding gas	–	Pure argon supply
Shielding gas flow rate	L/min	14
Inter-pass temperature	°C	110–150
Wire speed	mm/s	55
Arc running speed	mm/s	4.1
Delay between layer-to-layer deposition	min	3
Heat input	kJ/mm	0.2601
Average thickness of the developed HDSS plate	mm	8.54 ± 0.13

Abbreviations: GMAW: Gas metal arc welding; HDSS: Hyper-duplex stainless steel; WAAM: Wire arc additive manufacturing.

2.2. Microstructural characterization

For microstructure analysis, samples of 20 mm × 20 mm were extracted from three locations—top, middle, and bottom of the WAAM-fabricated HDSS wall (Figure 4)—using electrical-discharge-machining wire cutting. The samples were polished with silicon carbide papers (200–2,000 grit), followed by polishing with an alumina–silica slurry on velvet cloth for 10–15 min to achieve a mirror finish. Etching was performed with a 40% NaOH solution at 6 V direct current for 30 s, in accordance with ASTM A890-4A. The microstructure was analyzed using an optical microscope (Zeiss Axio inverted microscope, Germany) and a scanning electron microscope (Thermo Fisher FEI QUANTA 250 FEG, United States of America [USA]) coupled with EDS. EBSD analysis (JSM-IT800(SHL), JEOL, Japan) was performed with a step size of 0.05

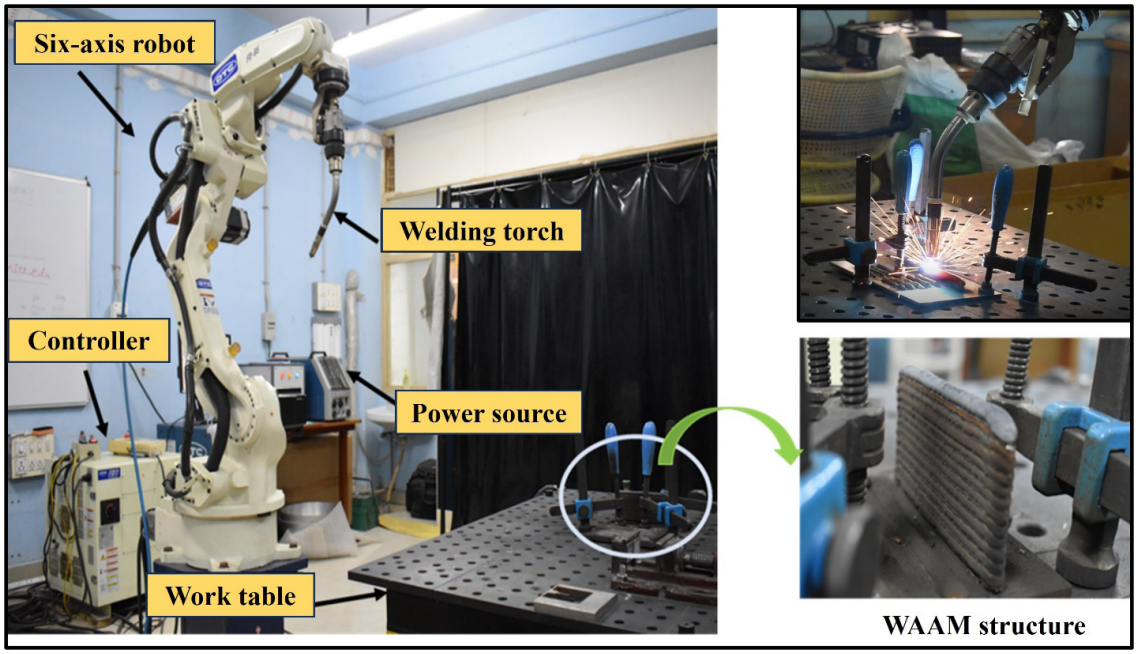

Figure 1. Gas metal arc welding (GMAW)-based wire arc additive manufacturing (WAAM) setup for developing a plate using UNS S32707 hyper-duplex stainless steel filler wire

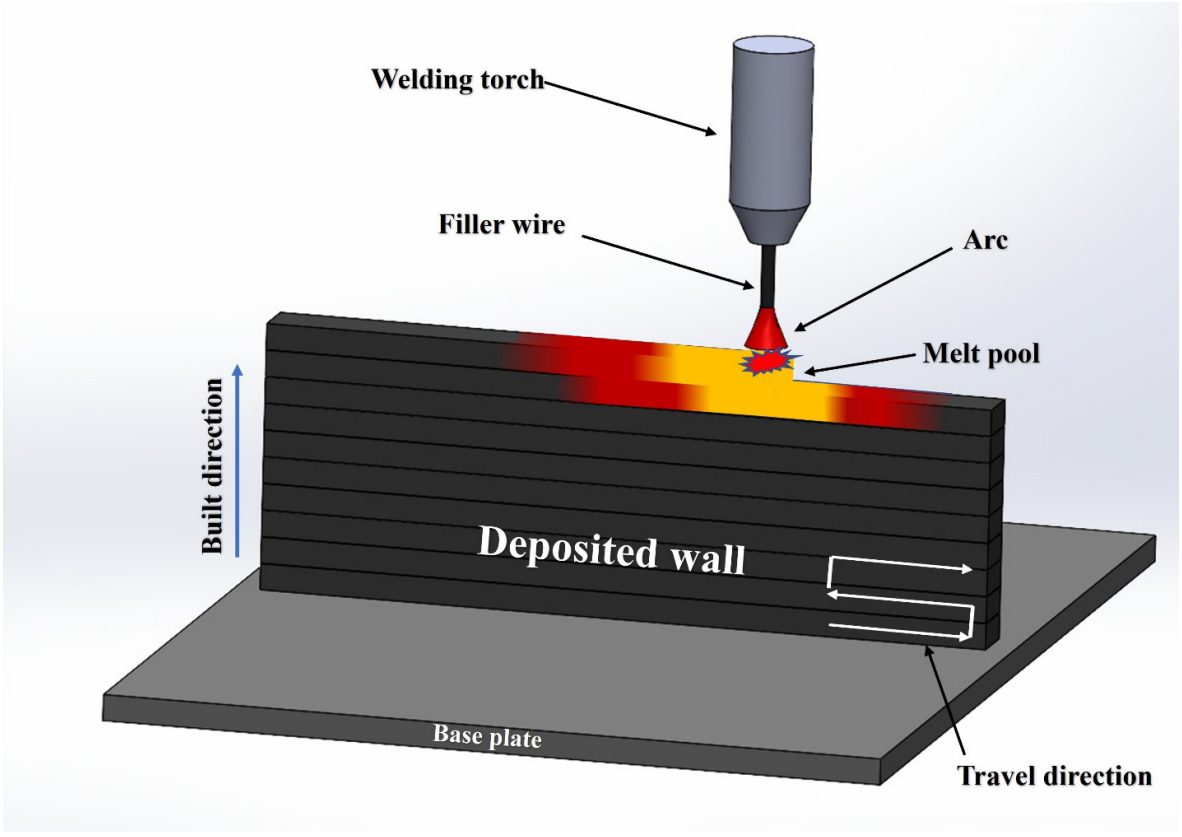

Figure 2. Schematic representation of the wire arc additive manufacturing deposition process

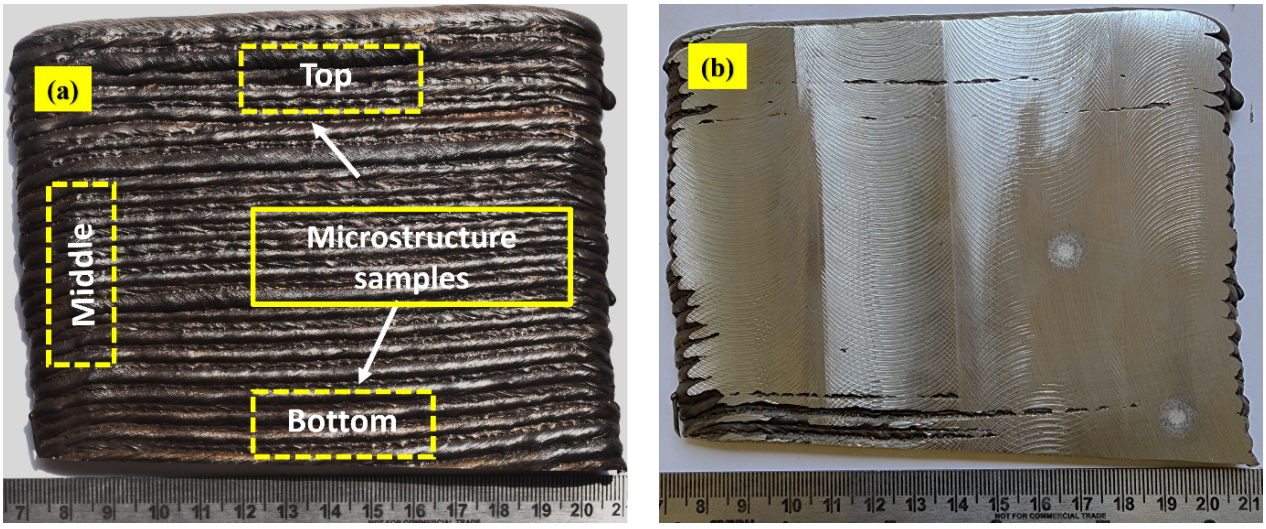

Figure 3. Images of the GMAW-based WAAM–fabricated UNS S32707 HDSS wall. (a) In as-deposited state. (b) After computer numerical control grinding. Abbreviations: GMAW: Gas metal arc welding; HDSS: Hyper-duplex stainless steel; WAAM: Wire arc additive manufacturing.

Table 2. Material composition of the UNS S32707 HDSS (wt.%)

HDSS	Cr	Ni	Mo	Mn	Si	P	C	S	N	PREN
Filler metal (%)	27.00	6.50	5.000	1.00	0.420	0.030	0.029	0.010	0.400	49.00
WAAM plate (%)	26.94	6.39	4.685	0.87	0.313	0.019	0.018	0.001	0.303	47.24

Abbreviations: HDSS: Hyper-duplex stainless steel; PREN: Pitting resistance equivalent number; WAAM: Wire arc additive manufacturing.

to examine grain orientation, phase distribution, and secondary precipitates, with TSL OIM software (version 9, TexSEM Laboratories, Inc., USA) used to analyze pole figures, kernel average misorientation (KAM), and inverse pole figures. X-ray diffraction (XRD) analysis (Bruker D8 Advance, Panalytical X Pert DEL, Germany) was employed to confirm the phases present. Ferrite content was measured using a ferritescope (FMP30, Helmut Fischer GmbH, Germany) at multiple points across the as-deposited wall surface. To supplement the ferritescope measurements, which have limited precision due to sensitivity to surface conditions and probe positioning, the ferrite volume fraction was also quantified from optical micrographs using image analysis software (ImageJ, National Institutes of Health, USA) following ASTM E1245 standards. Grain size was determined from EBSD data using the equivalent circle diameter method in accordance with ASTM E2627. Using the chemical composition obtained from OES, PREN was calculated as:

$$PREN = Cr + 3.3(Mo + 0.5W) + 16N \text{ (wt.\%)} \quad (2)$$

2.3. Tensile behavior and hardness testing

To study the anisotropic behavior of the WAAM-fabricated HDSS, micro-tensile specimens were extracted in three orientations: 0° (horizontal), 45° (diagonal), and 90° (perpendicular) relative to the build direction (Figure 4). The micro-tensile specimens had a gauge length of 5 mm, a gauge width of 1.25 mm, and a thickness of 0.8 mm. Three specimens were tested in each orientation. The specimen surfaces were polished with emery sheets to remove surface defects. Micro-tensile tests were performed on an Instron universal testing machine (UTM, 100 kN capacity; Instron 8801, USA) at a crosshead speed of 1 mm/min, corresponding to a strain rate of 2.78×10^{-4} s^{-1}. A clip-on extensometer was used to measure the yield strength of the samples. To validate the micro-tensile results and confirm their representativeness of the bulk WAAM-fabricated HDSS wall behavior, three full-sized tensile specimens were tested in the horizontal direction (0°) as per ASTM E8/E8M-16 standards. These bulk specimens had a standard gauge length of 25 mm and were tested on the above-

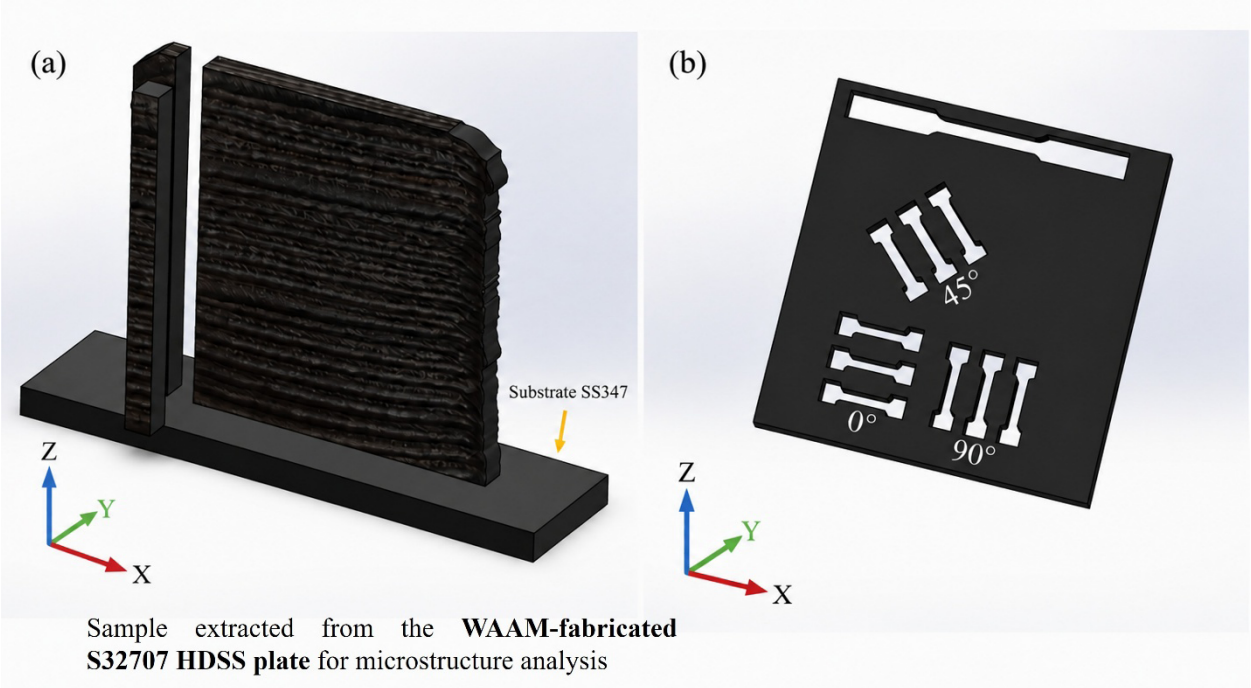

Figure 4. Computer-aided design representation of (a) samples cut from WAAM-fabricated HDSS for microstructural characterization and (b) micro-tensile and bulk tensile testing
Abbreviations: HDSS: Hyper-duplex stainless steel; WAAM: Wire arc additive manufacturing.

mentioned UTM machine. Fractography was performed on the fractured bulk tensile specimens (0° orientation) using SEM to examine fracture surface features. Microhardness was measured using a Vickers hardness tester (HM-200, Mitutoyo, Japan) following ASTM E384-17, with a load of 500 *g* (4.9 N) and a 10-s dwell time. Indentations were made at regular vertical intervals along the centerline of the wall cross-section.

2.4. Electrochemical corrosion testing

Electrochemical corrosion tests were conducted using a 3.5 wt.% NaCl solution at room temperature with an Ivium Vertex One (Ivium Technologies, the Netherlands) potentiostat in a three-electrode configuration, the sample as working electrode (1 cm^2 exposed area), a saturated calomel electrode (SCE) as reference, and a platinum electrode as counter electrode. Prior to testing, each sample was polished from 400 to 2,000 grit, finished with alumina–silica slurry, rinsed with distilled water, and degreased with ethanol. Each specimen was first stabilized at its open-circuit potential (OCP) for one hour (3,600 s) at 1-s sampling intervals to ensure steady-state conditions prior to polarization. Potentiodynamic polarization scans with Tafel analysis were then performed at a scan rate of 50 mV/s with a potential step of 10 mV, sweeping from 0.247 V to −0.752 V vs. SCE (i.e., from +500 mV to −500 mV relative to OCP). The corrosion potential (E_{corr}) was determined from zero current crossing, and the corrosion current density (j_{corr}) was obtained through Tafel extrapolation, using linear regions of anodic and cathodic branches in the overpotential range from ±30 to ±120 mV. The corrosion rate was determined using Faraday's law, with an equivalent weight of 25.8 g/equiv and a density of 7.86 g/cm^3 for HDSS. EIS (Ivium, Vertex One, Netherlands) was performed at OCP with a sinusoidal perturbation of 10 mV amplitude in the frequency range of 0.1 Hz–100 kHz with six logarithmically spaced points in frequency. The EIS data were analyzed using Iviumsoft software (Ivium Technologies). Nyquist and Bode plots were plotted to evaluate the capacitive response and passive film behavior.

3. Results and discussion

3.1. Microstructural analysis

The primary challenge in developing HDSS through WAAM is achieving a balanced volume fraction of austenite and ferrite while suppressing secondary phases. During the WAAM process, the high-energy heat source interacts with the wire feedstock, which generates complex thermal cycles involving rapid melting, solidification, and cooling, resulting in microstructural variations

along the build direction.[34] Figure 5 presents the optical micrographs of the WAAM-fabricated UNS S32707 HDSS at different locations (bottom, middle, and top; Figure 3a) and magnifications. The microstructure revealed an approximately equal fraction distribution of austenite and ferrite, in accordance with ASTM A890 standards. The austenite (γ) appeared as discrete, island-shaped regions outlined by bright contrast along the grain interfaces, distributed within a continuous ferritic (α) matrix (Figure 5d). Within the ferrite, austenite is present in three characteristic morphologies: grain-boundary austenite (GBA) as elongated allotriomorphic structures decorating grain boundaries (Figure 5f), Widmanstätten austenite (WA) as side-plate structures nucleating from GBA and growing into the ferrite matrix, and intragranular austenite (IGA) as fine particles nucleating independently within the ferrite grains (Figure 5d). The differences in microstructures obtained at different wall heights are attributed to the CCTH due to the remelting of neighboring layers during the WAAM process, as reported by Kannan *et al.*[24] With increasing wall height, the ferrite bands progressively decreased in extent, accompanied by the formation of more extensive austenite, consistent with the observations of Nikam *et al.*[35] for cold metal transfer–based SDSS. This is due to heat build-up during layer-by-layer deposition, resulting in higher preheat temperatures at higher wall heights and slower cooling rates, both of which are favorable for austenite transformation. The ferrite content measured using the ferritescope was 45%, 42%, and 38% in the bottom, middle, and top sections, respectively. These values were validated using optical micrographs in ImageJ (ASTM E1245), which showed ferrite fractions of 46.2 ± 2.1%, 43.5 ± 1.8%, and 39.1 ± 2.3% at the bottom, middle, and top, respectively, in agreement with the ferritescope data. The bottom layers exhibited finer ferrite and austenite structures due to the faster cooling rate and lower thermal gradient, with heat dissipated rapidly through the substrate (Figure 5e and 5f). Both the heat input and the cooling rate substantially influenced the phase transformation process. The same phenomenon was observed in DSS: an increase in the cooling rate delays the austenite transformation.[35] Cooling rate is an important parameter for microstructure development during solidification.[36] In the present study, the heat input was maintained at 0.2601 kJ/mm, and the cooling rate was controlled with a 3-min inter-layer delay, which balanced the phase fraction by moderating the austenite formation. The PREN value of 47.24, obtained from OES data using **Equation 2**, confirms that the GMAW-based WAAM–fabricated HDSS wall meets the corrosion resistance criteria of the National Association of Corrosion Engineers (NACE) for oil and gas applications (PREN > 40).

3.2. Scanning electron microscopy and elemental analysis

In HDSS, the relative stability of the two phases is governed by the partitioning of alloying elements between ferrite and austenite. Cr, Si, and Mo are ferrite stabilizers and partition preferentially into the δ-ferrite matrix, while Ni and Mn are austenite stabilizers and enrich the austenite phase. The cooling rate during solidification influences the diffusion of elements and, consequently, the final composition balance and phase morphology. SEM analysis with EDS area mapping was used to elucidate the microstructural relationships in the WAAM-fabricated HDSS. From the SEM image (Figure 6) and the corresponding EDS maps (Figure 7), the main alloying elements (Cr, Ni, Mo, Co, Mn, W, Si, Fe) were well distributed in δ-ferrite and γ-austenite regions. This confirms that the fast solidification and increased cooling time during deposition in the WAAM process provided sufficient time for diffusion, resulting in chemical homogeneity.

3.3. Phase analysis

The XRD diffractogram of the UNS S32707 HDSS sample (Figure 8) showed distinct Bragg peaks in the 2θ range of 20°–90°, indexed to austenite (γ, face-centered cubic [FCC]) and ferrite (α, body-centered cubic [BCC]) crystal structures. The γ-austenite reflections were accompanied by sharp, high-intensity peaks corresponding to the ferritic phase. No additional peaks corresponding to secondary phases (e.g., σ, χ, Cr_2N) were detected in the diffractogram. However, it should be noted that the absence of XRD peaks does not necessarily indicate the complete absence of secondary phases; rather, it indicates that any secondary phases present are below the detection limit of XRD (typically <2.5 vol.%). The trace amount of σ phase (~0.5%) detected using EBSD (Section 3.4) is consistent with this interpretation. The peak positions and relative intensities agree with the preferential development along the close-packed planes, specifically $(110)_{\alpha}$ and $(111)_{\gamma}$.[37]

3.4. Electron backscatter diffraction analysis

Electron backscatter diffraction analysis was conducted to quantify phase distribution (representing the local measurement), crystallographic orientation, grain-boundary character, and strain localization in the middle region of the WAAM-fabricated HDSS (Figures 9–14). Figure 9a presents the EBSD image quality map, i.e., the microstructural feature for the HDSS. The phase map in Figure 9b reveals a hyper-duplex microstructure comprising 52.1% ferrite (BCC/green region), 47.4% austenite (FCC/red region), and 0.5% σ phase (yellow region), confirming a well-balanced duplex structure. Notably, it was found that phase fractions differed along

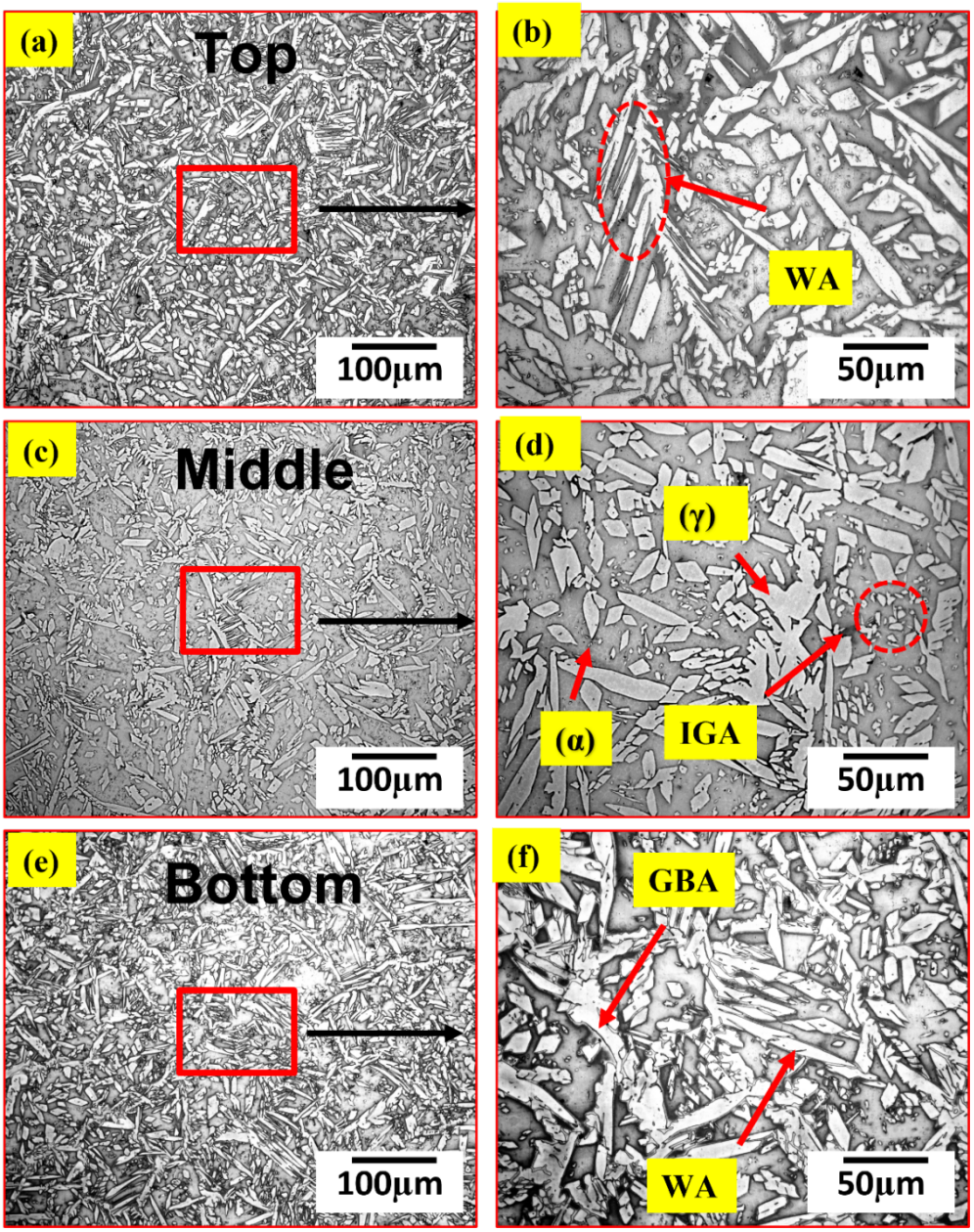

Figure 5. Microstructure images of WAAM-fabricated UNS S32707 HDSS along the build direction at different locations and magnifications: (a, b) top, (c, d) middle, (e, f) bottom. Scale bars: (left panels) 100 μm, (right panels) 50 μm
Abbreviations: GBA: Grain-boundary austenite; HDSS: Hyper-duplex stainless steel; IGA: Intragranular austenite; WA: Widmanstätten austenite; WAAM: Wire arc additive manufacturing.

the wall height, and fractions at other locations would differ according to the ferrite fractions described in Section 3.1. The σ phase occurred at grain boundaries and triple junctions, indicating that high-energy sites are conducive to nucleation. Other secondary phases, such as χ phase, γ_2, and Cr_2N, were not detected. The WAAM thermal cycle promotes phase evolution through the influence of diffusion kinetics and thermodynamic driving forces under non-equilibrium solidification. Ferrite solidifies first due to its lower free energy at elevated temperatures, followed by diffusion-controlled solid-state transformation of austenite, which nucleates at ferrite grain boundaries where solute segregation facilitates the transformation.[38] The σ phase forms due to the enrichment of Cr, Mo, and W

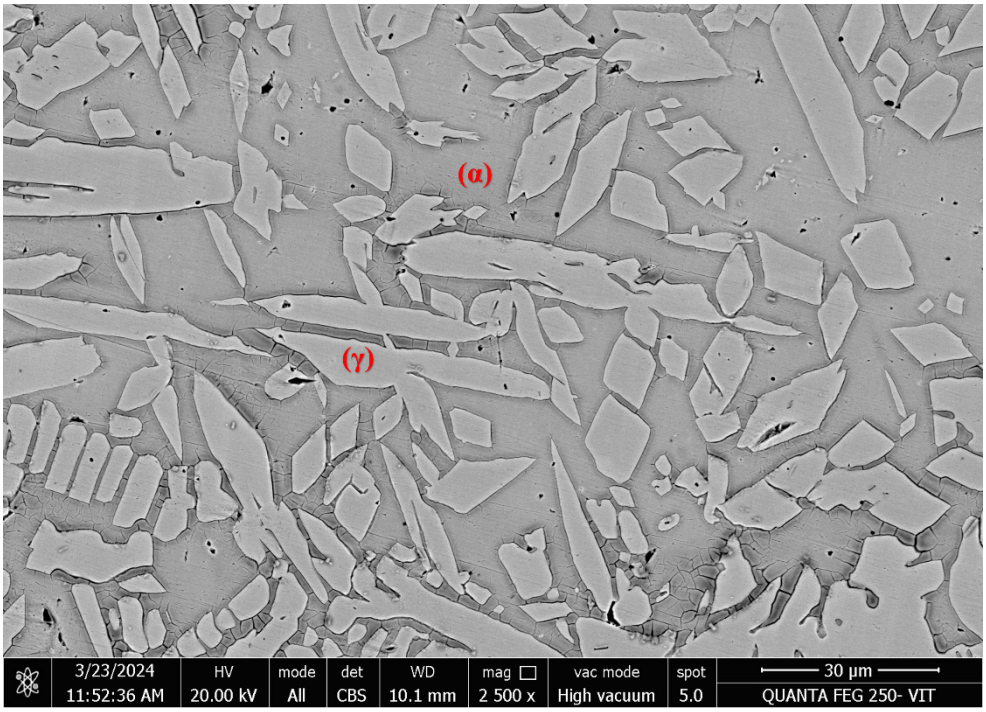

Figure 6. Scanning electron microscopy image of WAAM-fabricated UNS S32707 HDSS showing austenite (γ) and ferrite (α) phases. Scale bar: 30 µm
Abbreviations: HDSS: Hyper-duplex stainless steel; WAAM: Wire arc additive manufacturing.

at phase boundaries during the repeated thermal cycling of successive layer depositions. This stable intermetallic compound forms at temperatures between 600 °C and 1,000 °C.[39] The minimal occurrence of σ-phase in this study indicates that the maintained inter-pass temperature (110 °C–150 °C) and moderate heat input (0.2601 kJ/mm) effectively limited the time spent in the *σ*-formation temperature range. Similar thermal control strategies have been reported by Chiniforoush *et al.*,[40] who suppressed secondary phases in WAAM-fabricated DSS (ER 2209) by maintaining an interlayer temperature of 150 ± 10 °C. The absence of χ phase and Cr_2N precipitates may be attributed to the faster cooling experienced during the WAAM deposition process. The χ phase, being metastable, can transform into the more stable σ phase upon prolonged thermal exposure, while Cr_2N precipitates may dissolve or be suppressed due to nitrogen redistribution and reheating effects. These observations are consistent with the reported phase transformation behavior of high-chromium duplex and HDSS.[41] The orientation-image microscopy maps for the FCC, BCC, and *σ* phases are presented in Figure 10, showing the spatial distribution and crystallographic orientation of each phase.

The KAM distribution (Figure 9c) was analyzed to evaluate local strain accumulation and deformation heterogeneity.[42] The blue region corresponds to areas of low local misorientation (<1°), indicating a relatively low density of geometrically necessary dislocations, whereas red regions represent localized strain concentrations. The predominance of blue regions in the KAM map with a very small green region suggests that the WAAM-fabricated HDSS possesses a stable microstructure with limited residual strain localization.

The observed local misorientation is attributed to the cyclic thermal history associated with the WAAM process. Repeated heating and cooling cycles generate thermal expansion mismatches between the FCC austenite and BCC ferrite phases, while solidification shrinkage contributes to dislocation accumulation. Furthermore, the small amount of σ phase detected at grain boundaries may promote localized stress concentrations due to its crystallographic incompatibility with the surrounding matrix. Nevertheless, the overall low KAM value ranged from 0° to 4.97°, indicating that strain is distributed relatively uniformly throughout the microstructure. This observation is consistent with the fractographic analysis, which revealed a predominantly ductile fracture mode characterized by significant plastic deformation prior to failure.

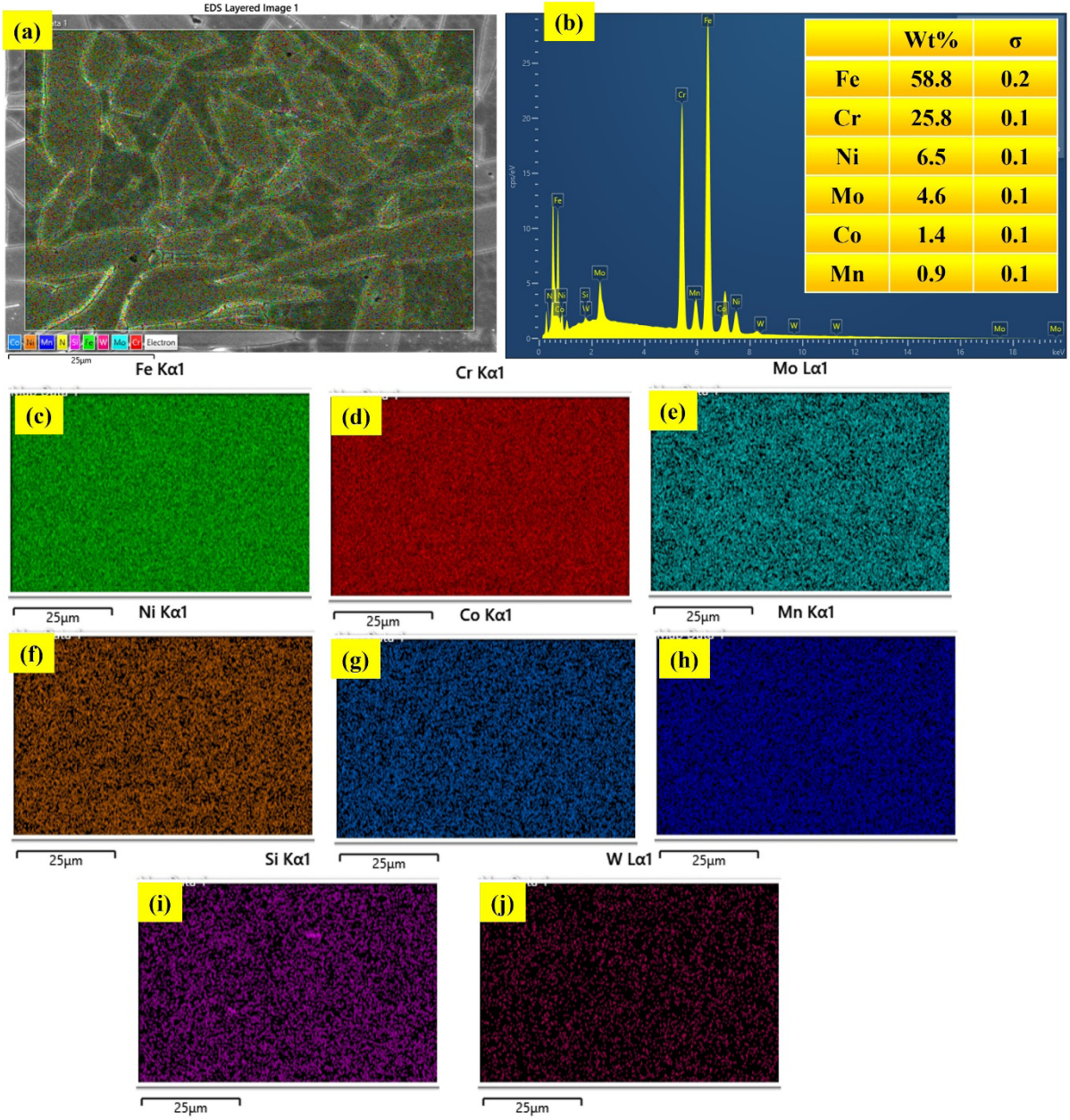

Figure 7. Energy-dispersive spectroscopy (EDS) elemental distribution maps showing the alloying elements (Cr, Ni, Mo, Co, Mn, W, Si, Fe) across δ-ferrite and γ-austenite regions. (a) EDS layered image. (b) EDS spectrum. (c) Fe Kα1. (d) Cr Kα1. (e) Mo Lα1. (f) Ni Kα1. (g) Co Kα1. (h) Mn Kα1. (i) Si Kα1. (j) W Lα1. Scale bar: 25 µm.

3.4.1. Crystallographic texture analysis

The inverse pole figures of the FCC and BCC phases are presented in Figure 11. The FCC phase showed grains oriented toward <001>II BD in the [001] plane, with an intensity of 2.07 multiple uniform distribution (MUD), representing weak texture; while the BCC phase showed strong texture with 4.25 MUD. From the literature,[43,44] it is attributed to the low degree of lattice freedom during solid-state transformation of the FCC phase from the BCC phase. BCC forms as the primary solidification phase and grows epitaxially along the direction of maximum heat extraction. The strong preferred orientation observed in the BCC phase is therefore associated with directional solidification under steep thermal gradients. During subsequent cooling, austenite (FCC) nucleates and grows within the ferrite

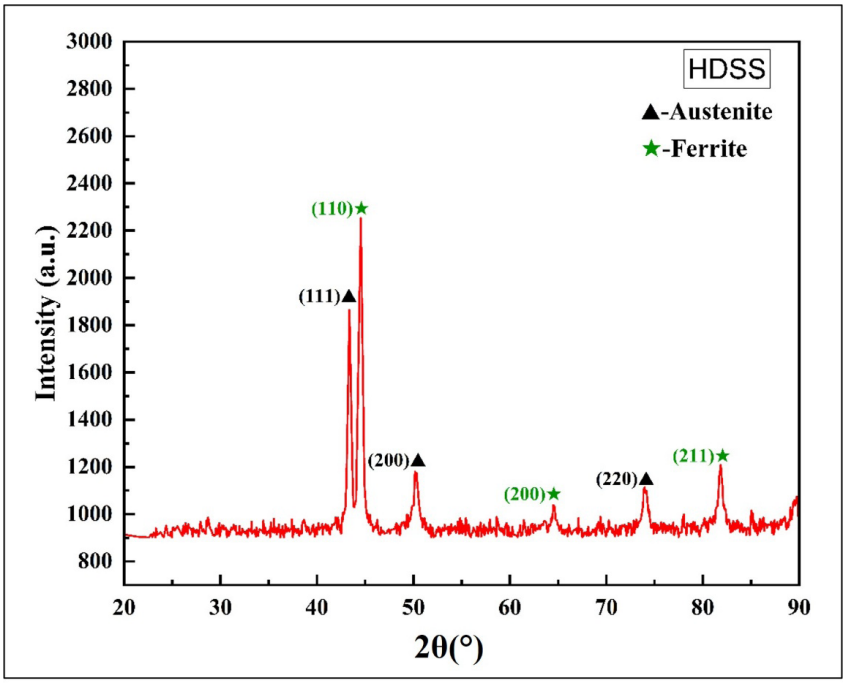

Figure 8. X-ray diffraction pattern of the GMAW-based WAAM–fabricated HDSS sample showing indexed peaks corresponding to α-ferrite (BCC) and γ-austenite (FCC)
Abbreviations: BCC: Body-centered cubic; FCC: Face-centered cubic; GMAW: Gas metal arc welding; HDSS: Hyper-duplex stainless steel; WAAM: Wire arc additive manufacturing.

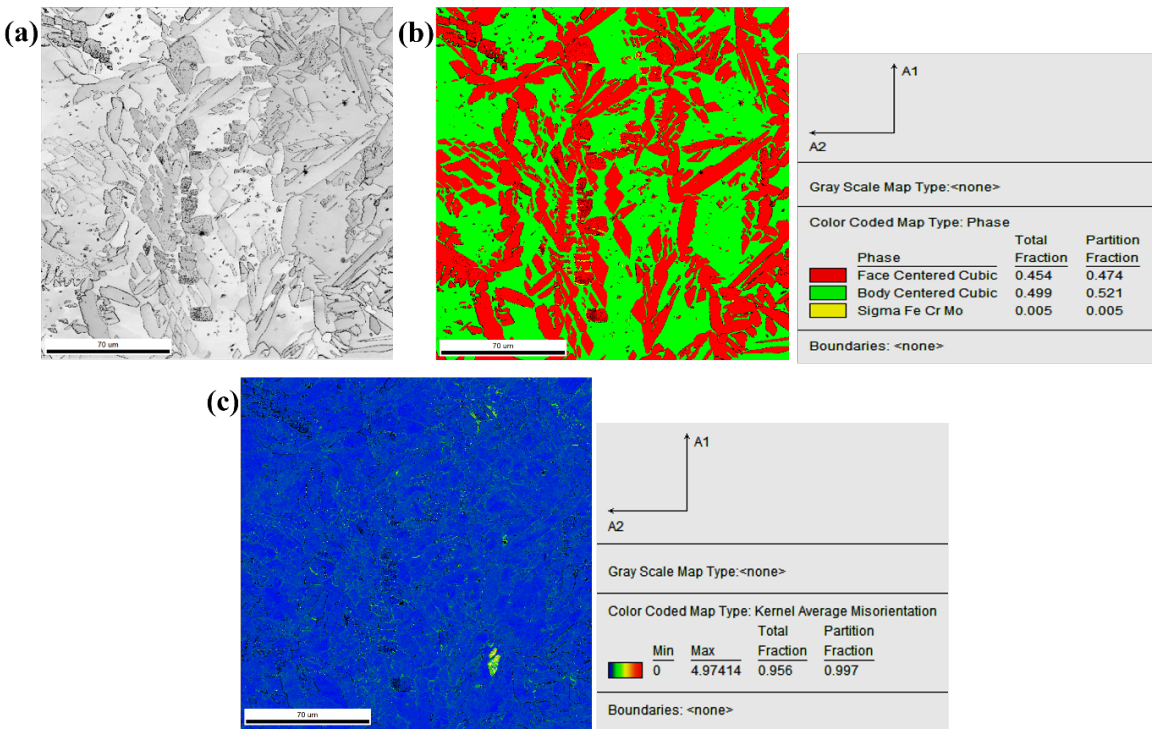

Figure 9. Electron backscatter diffraction analysis: (a) image quality map, (b) phase map, and (c) kernel average misorientation map. Scale bar: 70 μm.

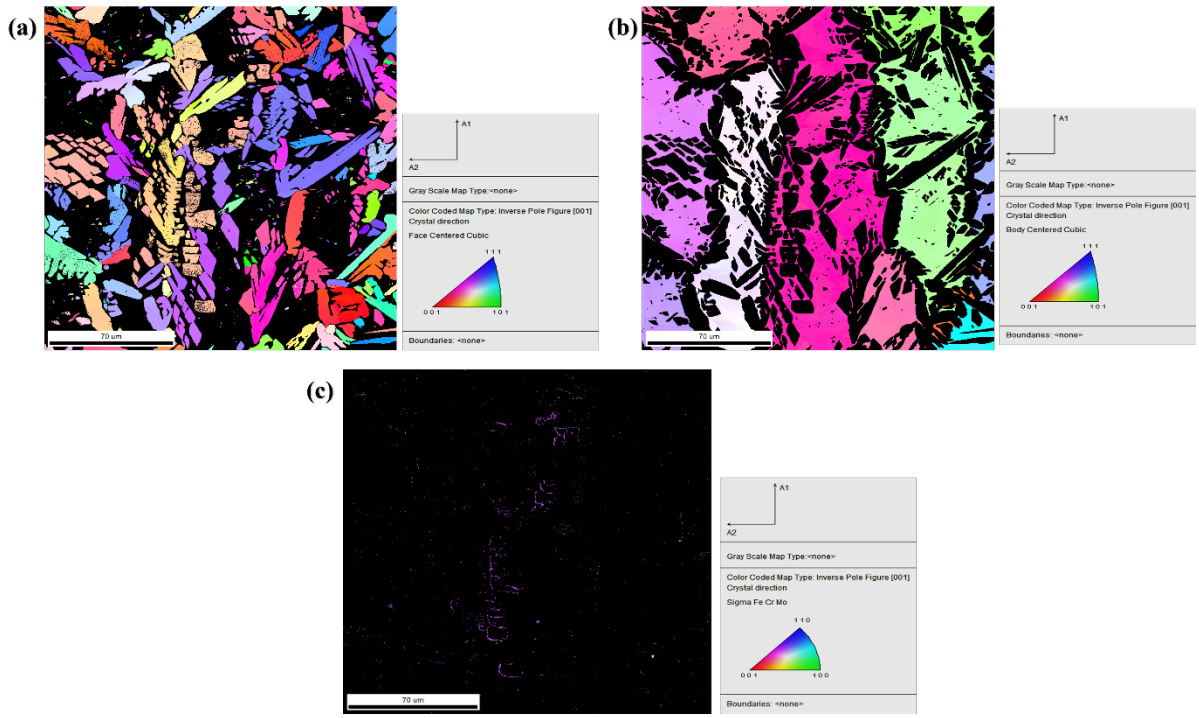

Figure 10. Orientation image microscopy maps: (a) Face-centered cubic (FCC), (b) body-centered cubic (BCC), and (c) σ phase. Scale bar: 70 µm.

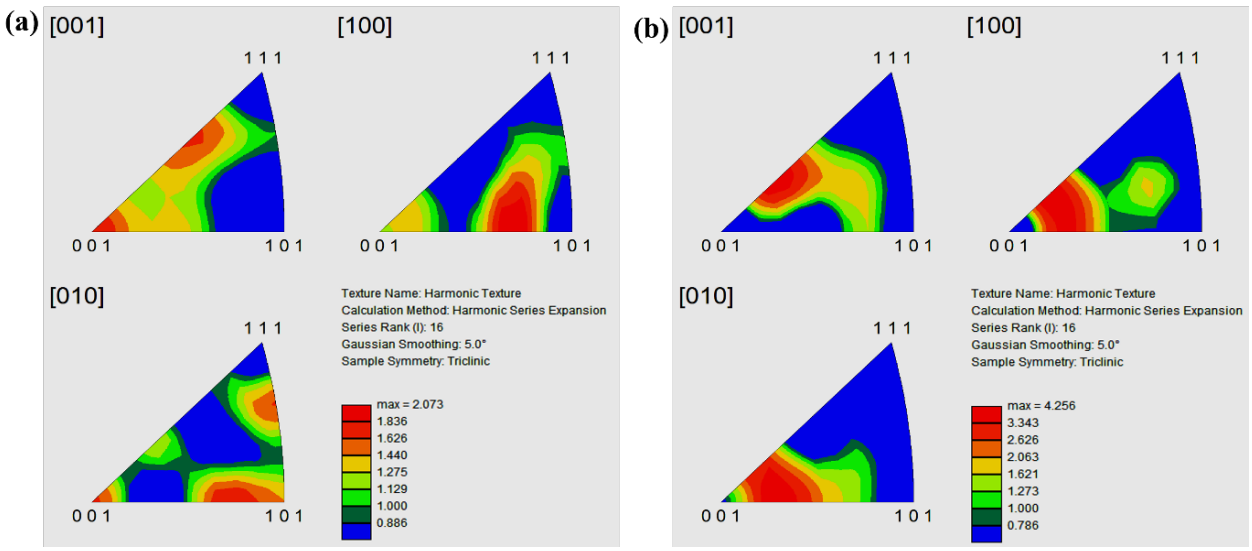

Figure 11. Inverse pole figures of (a) face-centered cubic (FCC) and (b) body-centered cubic (BCC)

matrix through a solid-state transformation, inheriting specific crystallographic orientation relationships from the parent ferrite. The ferrite-to-austenite transformation kinetics contribute to the restricted atomic mobility in FCC and thereby influence the microstructural phase balance.

The thermal gradient (G) and solidification growth rate (R) play a crucial role in determining grain morphology and texture evolution during WAAM. High G:R ratios

favor directional grain growth and texture development,[45] whereas repeated thermal history associated with subsequent layer deposition can promote recovery, grain refinement, and partial texture randomization.

The pole figures in Figure 12 show the [001], [111], and [110] planes corresponding to the FCC and BCC phases. The FCC phase exhibited a texture intensity of 8.67 MUD (Figure 12a), whereas the BCC phase showed a markedly higher maximum texture intensity of 21.91 MUD (Figure 12b). As previously mentioned, the increase in the ferrite texture intensity is caused by ferritization and reorientation of grains in the direction of the thermal gradient, while the decrease in the austenite texture intensity is caused by its dissolution during ferritization and partial static recrystallization.[46]

3.4.2. Grain size analysis

The grain size distributions for both FCC and BCC phases, determined from EBSD data using the equivalent circle diameter method in accordance with ASTM E2627, are presented in Figure 13. The FCC phase exhibited a finer average grain size of 14.7 μm compared to the BCC phase with an average grain size of 54.8 μm, reflecting the finer austenite grains produced by solid-state transformation and the coarser ferrite grains formed during primary solidification. This higher fraction of high-angle grain boundaries (HAGBs) in WAAM samples is due to finer grain refinement and grain dislocation pinning. In DSS, the grain size is finer than that of austenite and ferritic single-phase stainless steels. This is attributed to the dual phase and the pinning effect of the ferrite and austenite grains, which restricts the growth of the partner's grains.[47] This finding is consistent with research on stainless steels.

3.5. Grain boundary distribution

Figure 14 presents the grain boundary misorientation for both FCC and BCC phases. Boundaries with misorientations of 2°–15° were classified as low-angle grain boundaries (LAGBs), and those between 15°–180° as HAGBs. The LAGB fractions in FCC and BCC were 63.44% and 92.63%, while HAGB fractions were 36.56% and 7.37%, respectively. The predominance of LAGBs is linked to the accumulation and reorganization of dislocations into sub-grain structures during successive WAAM thermal cycles. Rapid thermal cycling and steep thermal gradients facilitate recovery and substructure formation but are insufficient to promote extensive boundary migration or recrystallization, limiting HAGB formation.[48]

In the FCC austenite phase, a high HAGB fraction (36.6%) was observed, indicating greater grain subdivision and potential recrystallization during the repeated thermal cycles associated with the WAAM process. In contrast, the BCC ferrite phase exhibited a dominant LAGB fraction (~92.6%), suggesting extensive sub-grain formation through dislocation rearrangement and recovery, with limited grain-boundary migration.

The high density of LAGBs in ferrite reflects the

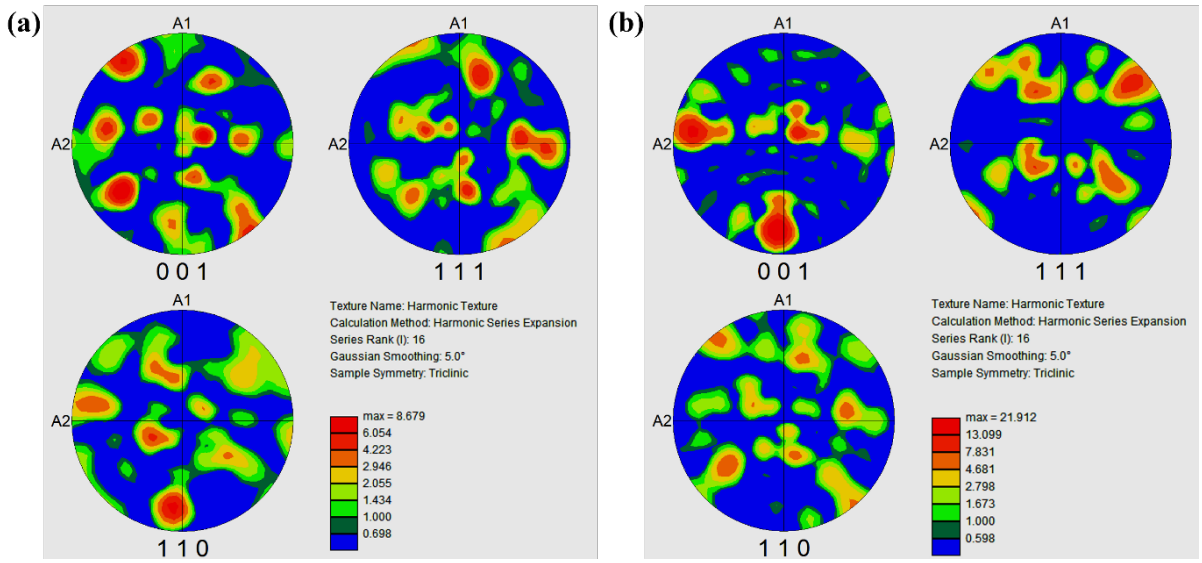

Figure 12. Pole figures of (a) face-centered cubic (FCC) and (b) body-centered cubic (BCC)

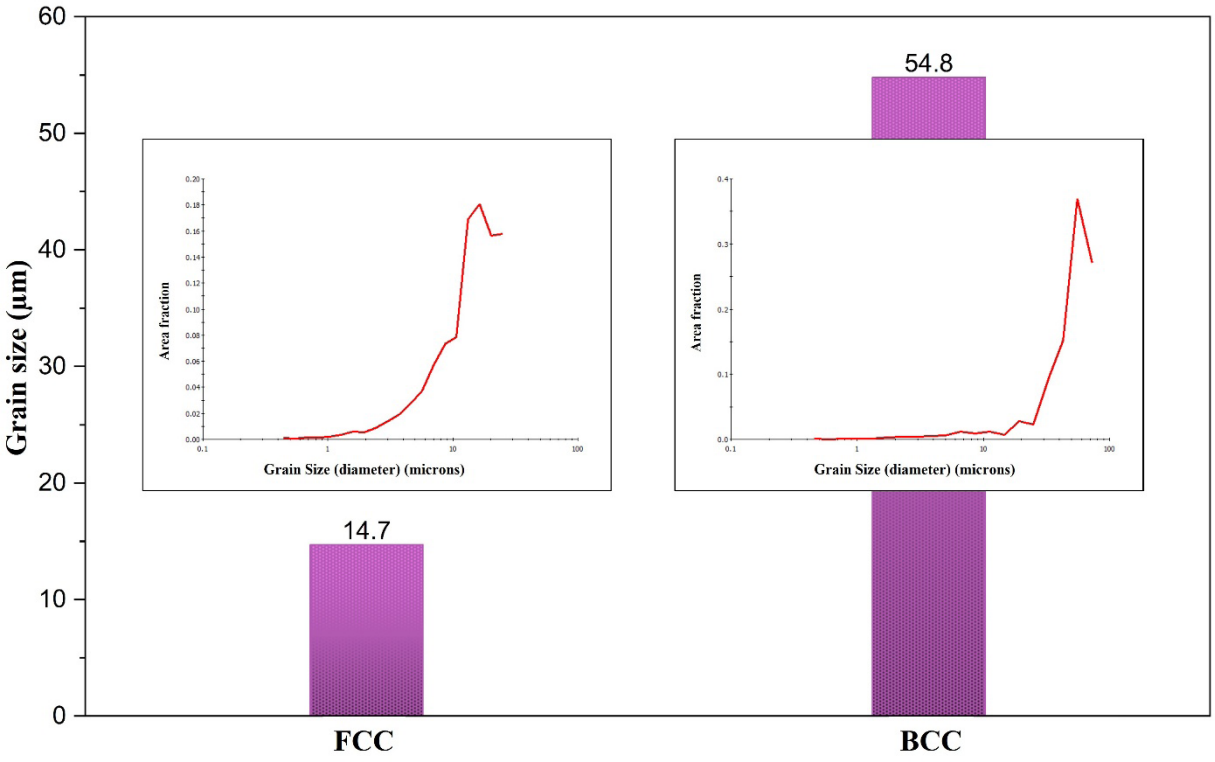

Figure 13. Electron backscatter diffraction grain size distributions for face-centered cubic (FCC) and body-centered cubic (BCC) phases

accumulation and stabilization of dislocation structures generated during cyclic thermal exposure. These boundaries act as effective barriers to dislocation motion, thereby contributing to strengthening through impeded slip transfer while reducing localized stress concentrations.[36] Consequently, the predominance of LAGBs in the ferrite phase is expected to enhance strength and hardness. Conversely, the higher HAGB fraction in the austenite phase facilitates more effective slip transmission and strain redistribution across grains, thereby promoting plastic deformation and contributing to the overall ductility of the WAAM-fabricated HDSS.

3.6. Microhardness

Microhardness indentations were performed at regular intervals along the centerline of the cross-section parallel to the build direction. As shown in Figure 15, the average hardness over the full wall height was 334 ± 20 HV, indicating a uniform mechanical behavior. Localized peak hardness values were, however, recorded in some zones, close to 390 HV, especially at the bottom layers near the substrate and in isolated interlayer zones. The increased hardness is attributed to locally increased cooling rates near the substrate, resulting in a finer microstructure with a higher ferrite fraction and higher dislocation density. Further localized enrichment of Cr and Mo at interlayer boundaries may promote minor σ-phase nucleation, which contributes to hardness spikes. The difference between the average and peak values is attributed to the inherent microstructural heterogeneity induced by thermal gradients during WAAM deposition. While the bottom layers are quenched faster through the substrate, the upper layers accumulate heat and form coarser and more austenite-rich structures. The variation in microhardness directly correlates with the observed microstructural gradient. A higher volume fraction of austenitic phases (GBA, IGA, WA) generally contributes to increased hardness owing to the solid solution strengthening effects of nitrogen in austenite, while the ferritic regions exhibit comparatively lower hardness. The progressive increase in austenite content from bottom to top (38–45% ferrite) corresponds to a slight decrease in average hardness in the upper regions, consistent with the softer austenitic phase becoming more dominant. Similar behavior was observed in SDSS developed through WAAM.[35] The microstructural variation is a direct consequence of the CCTH during

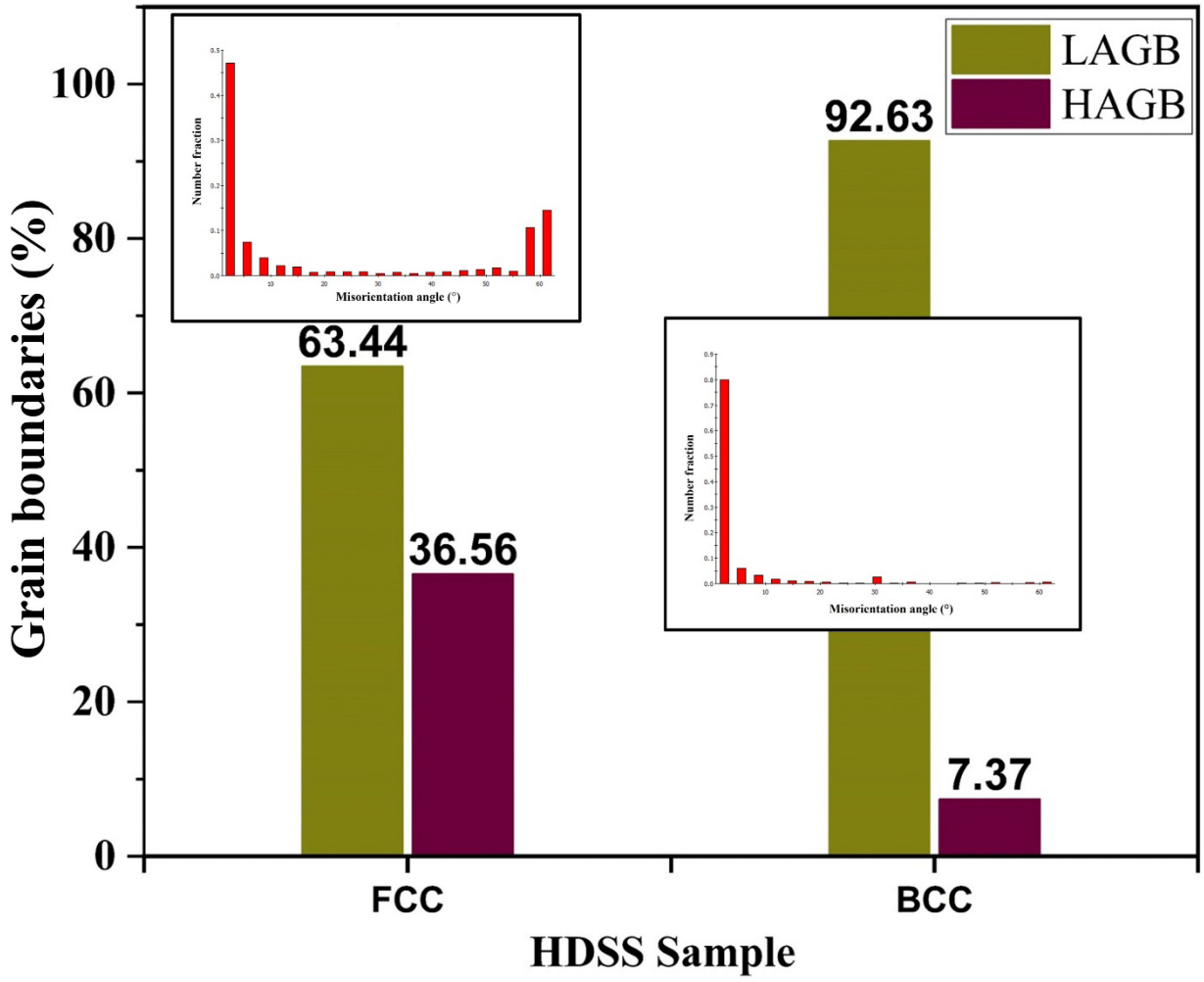

Figure 14. Grain boundary misorientation histogram for face-centered cubic (FCC) and body-centered cubic (BCC) phases showing low-angle grain boundary (LAGB) and high-angle grain boundary (HAGB) distributions

fabrication,[39] and the cumulative preheating effect from previously deposited layers facilitates ferritic-to-austenitic transformation in upper regions.[49]

3.7. Tensile behavior of WAAM-fabricated HDSS

Micro-tensile tests were conducted on the WAAM-fabricated HDSS wall in three orientations: horizontal (0°), diagonal (45°), and vertical (90°) relative to the build direction. The results are given in Figure 16 and Table 3. The specimens with 0° orientation showed the highest ultimate tensile strength (UTS; 943 MPa) and the highest total elongation (45.2%). The 45° specimens reported a UTS of 935 MPa with 44.5% elongation, and the 90° specimens reported a UTS of 927 MPa with 46.7% elongation. It should be noted that the micro-tensile specimens had a small gauge length, which could influence the total elongation because the specimen size effects are significant at sub-standard gauge lengths. To account for the absence of an extensometer, the uniform plastic elongation was estimated by subtracting the elastic component from the total elongation, yielding uniform plastic elongations of 44.7%, 44.0%, and 46.2% for the 0°, 45°, and 90° orientations, respectively. The elastic component is calculated as:

$$\varepsilon e = \sigma UTS/E \quad (3)$$

where $E \approx 200$ GPa for DSS.

The tested micro-tensile and bulk tensile specimens are shown in Figure 17. To validate the micro-tensile data, three bulk tensile specimens (ASTM E8/E8M-16, horizontal direction) were tested, yielding a UTS of 937 ± 7 MPa and a 0.2% proof (yield) strength of 764 MPa. The good

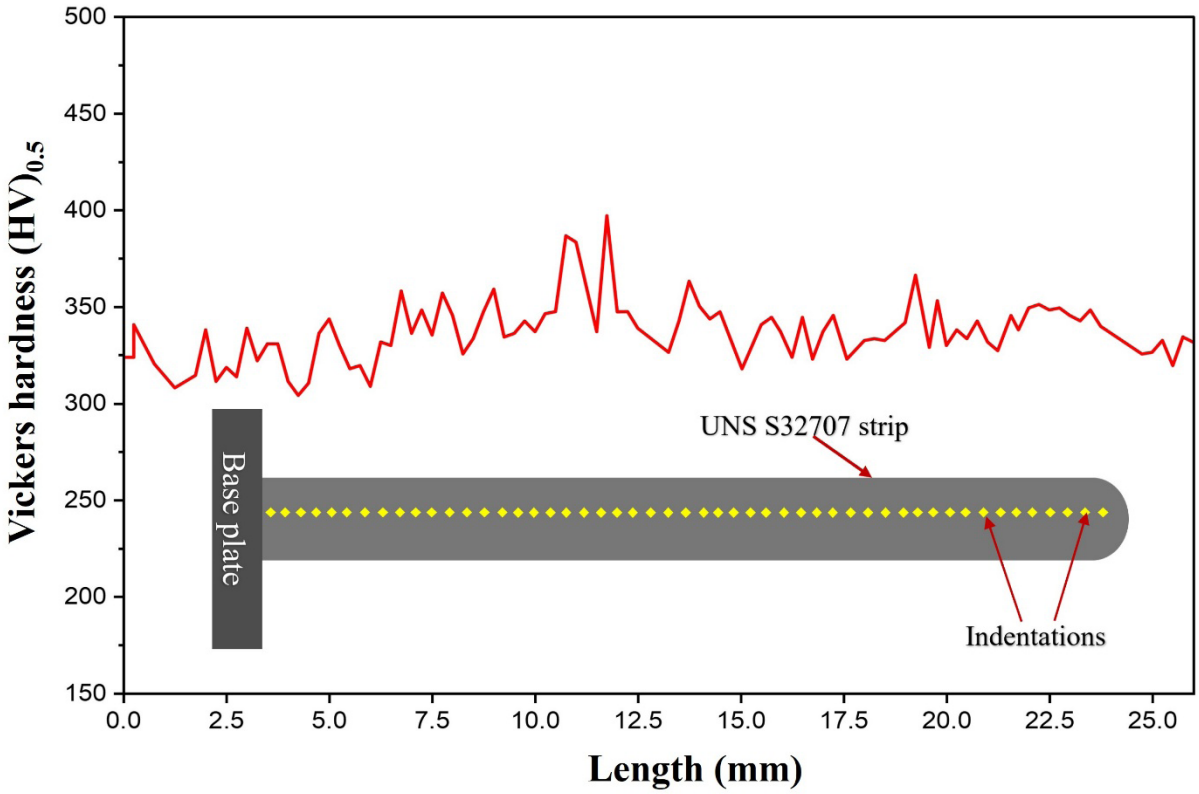

Figure 15. Microhardness profile along the centerline of the wire arc additive manufacturing–fabricated hyper-duplex stainless steel wall from bottom to top, showing the average and localized peak values

agreement between micro-tensile and bulk tensile results confirms that the micro-tensile data are representative of the overall WAAM-fabricated HDSS wall properties rather than being dominated by local heterogeneity. The tensile properties of the WAAM-fabricated HDSS compare favorably with those produced using other methods: as-cast HDSS (ASTM A-890 Grade 7A, ~920 MPa UTS),[10] PIM (761 MPa),[15] and SLM (901 MPa).[16] A comparison with literature values is summarized in Table 4. The slight mechanical anisotropy observed is correlated with the microstructural gradient along the build height. The higher strength in the 0° direction is associated with the finer, more equiaxed grain structure formed along the build direction, where solidification dynamics produce a favorable grain morphology. This improved strength is attributed to enhanced grain boundaries and the formation of higher grain boundaries through pinning and the Hall–Petch mechanism.[45] The slightly reduced strength at 90° is attributed to the transverse orientation crossing multiple interlayer boundaries, which experience different thermal histories. Importantly, the consistently high elongation values (>44%) across all orientations confirm that the WAAM process effectively suppressed the formation of embrittling phases (Cr_2N, σ, χ), maintaining the excellent ductility characteristic of properly balanced duplex microstructures.

Table 3. Average micro-tensile properties of GMAW-based WAAM–fabricated UNS S32707 HDSS

Property	Unit	0° (horizontal)	45° (diagonal)	90° (vertical)
UTS	MPa	943	935	927
Total elongation	%	45.2	44.5	46.7
Uniform plastic elongation	%	44.7	44.0	46.2

Note: Three samples per orientation.
Abbreviations: GMAW: Gas metal arc welding; HDSS: Hyper-duplex stainless steel; UTS: Ultimate tensile strength; WAAM: Wire arc additive manufacturing.

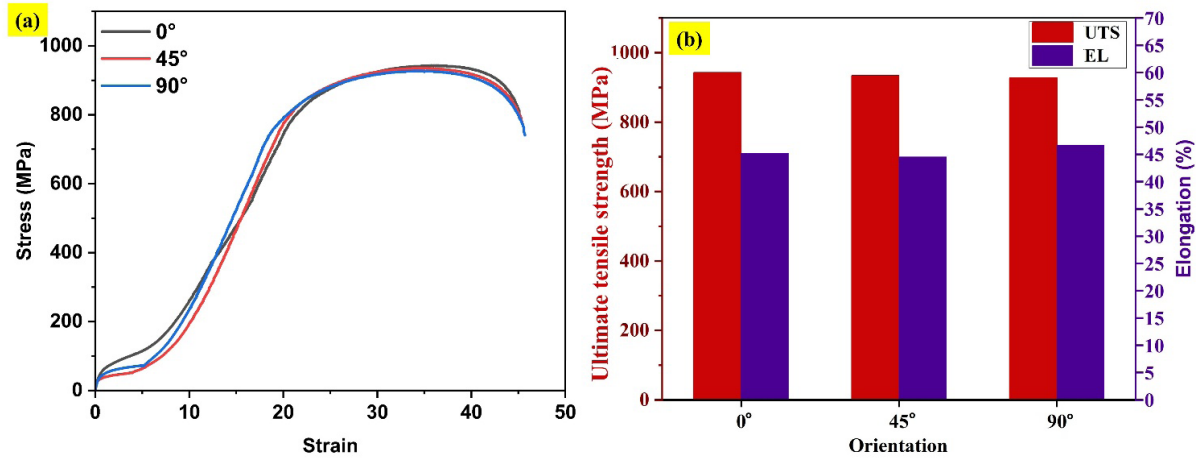

Figure 16. Micro-tensile behavior of WAAM-fabricated HDSS at 0°, 45°, and 90°. (a) Stress–strain curves. (b) Ultimate tensile strength (UTS) and elongation (EL) comparison.
Abbreviations: HDSS: Hyper-duplex stainless steel; WAAM: Wire arc additive manufacturing.

Table 4. Comparison of mechanical properties of UNS S32707 HDSS produced by different methods

Processing route	UTS (MPa)	YS (MPa)	Elongation (%)	Reference
As-cast (ASTM A890)	~920	–	–	[10]
PIM	761	529	14.0	[14]
SLM	901	658	36.4	[15]
GMAW-based WAAM (this work)	937±7	764	45.2	–

Abbreviations: GMAW: Gas metal arc welding; HDSS: Hyper-duplex stainless steel; PIM: Powder injection molding; SLM: Selective laser melting; UTS: Ultimate tensile strength; WAAM: Wire arc additive manufacturing; YS: Yield strength.

3.8. Fractography analysis

Figure 18 shows the fractographs of the bulk tensile specimen (0° orientation, fractured at 937 MPa) at different magnifications. The fracture surfaces revealed a predominantly ductile mode of failure, with numerous fine dimples resulting from micro-void nucleation, growth, and coalescence. Extensive dimple patterns confirm significant plastic deformation prior to failure, consistent with the high elongation values observed in tensile testing. Similar ductile fracture behavior has been reported in SDSS produced using DED.[50] The voids are primarily formed at the interfaces between ferrite and austenite phases and at inclusion sites, where the differences in mechanical properties between the two phases promote strain localization and void nucleation. The fine dimple size is consistent with the fine-grained, well-balanced duplex microstructure observed in the EBSD analysis, confirming that the absence of large brittle precipitates prevented premature cleavage fracture.

3.9. Potentiodynamic polarization studies

Kinetics of electrochemical corrosion were investigated using the polarization technique.[51] To evaluate corrosion performance, two tests were conducted: a non-destructive test (EIS) and a destructive test (potentiodynamic polarization). The polarization curve depicted the relationship between current density and potential. Figure 19 shows the polarization curve of HDSS. The electrochemical parameters comprising E_{corr}, j_{corr}, and Tafel slopes are listed in Table 5.

The E_{corr}, determined by interpolation, was −0.0424 V vs. SCE. Tafel extrapolation of the linear anodic and cathodic branches yielded an anodic Tafel slope (β_a) of 0.229 V/dec and a cathodic Tafel slope (β_c) of 0.689 V/dec. The average corrosion current from both branches was I_{corr} = 7.222 × 10−6 A (exposed area = 1 cm²). The corrosion rate was 0.07877 mm/year. The polarization resistance was computed via the Stern–Geary equation:

$$R_p = B/j_{corr} \quad (4)$$

where $B = \beta_a\beta_c/[2.303(\beta_a + \beta_c)]$, and the calculated R_p was 1.034×10^4 Ω·cm².

The Tafel slopes of 0.229 and 0.689 V/dec are within the typical range for passivating DSS, where mixed activation–diffusion control leads to slopes above the theoretical

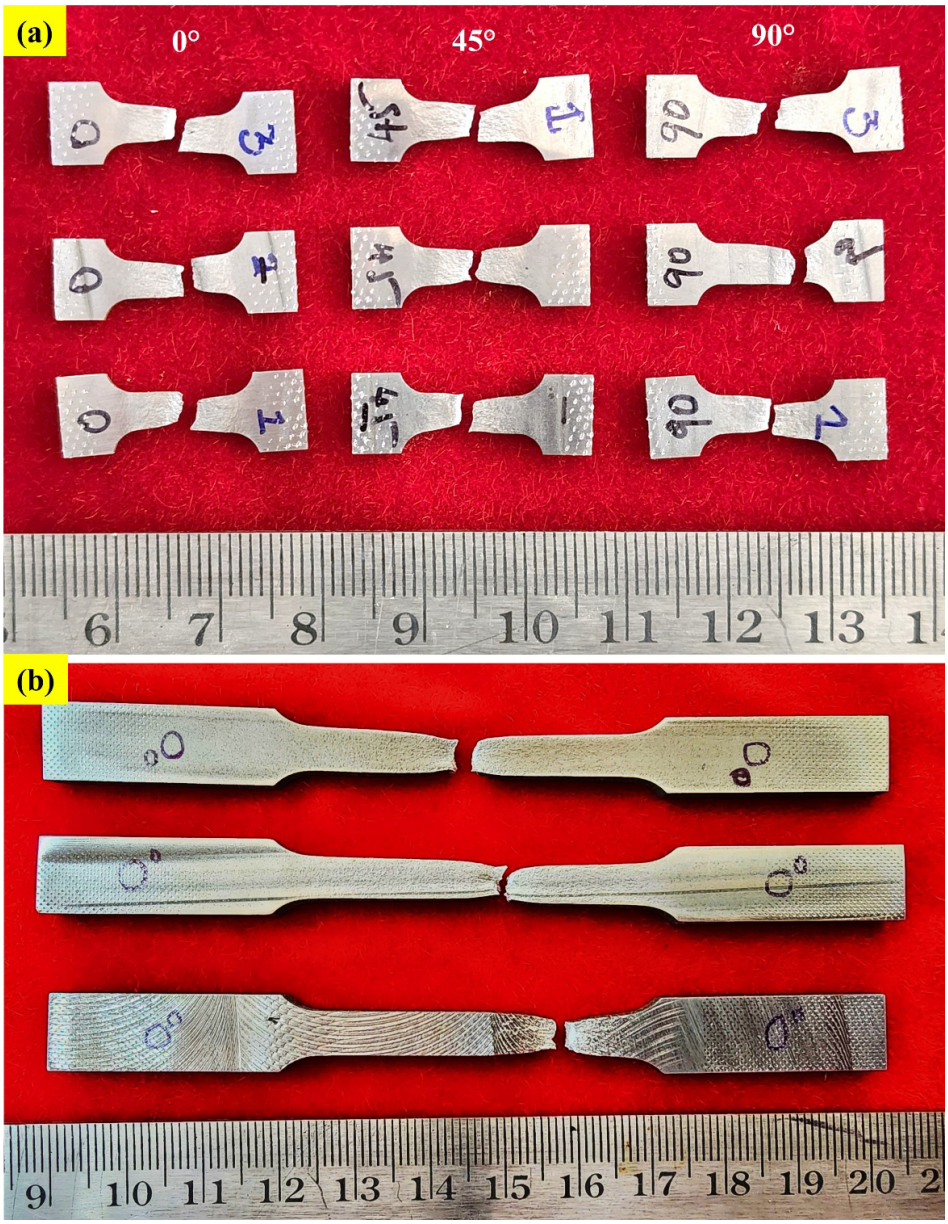

Figure 17. Fractured samples of GMAW-based WAAM–fabricated UNS S32707 HDSS: (a) micro-tensile specimens and (b) bulk tensile specimens
Abbreviations: GMAW: Gas metal arc welding; HDSS: Hyper-duplex stainless steel; WAAM: Wire arc additive manufacturing.

120 mV/dec for purely activation-controlled reactions.[50] The near-symmetry of the anodic and cathodic slopes indicates similar kinetic barriers for metal dissolution and cathodic oxygen reduction. The E_{corr} of −0.0424 V vs. SCE is consistent with the electrochemical behavior of Cr–Mo–N stainless steels, forming stable Cr_2O_3-based passive films in 3.5 wt.% NaCl. The corrosion rate of 0.0788 mm/year confirms good uniform corrosion resistance in the as-deposited condition; this value is lower than those reported for as-cast DSS grades[52] and comparable to WAAM-fabricated SDSS.

3.10. Open-circuit potential over time

Prior to polarization testing, the OCP of the WAAM-fabricated HDSS sample was monitored for 3,600 s (60 min) at 1-s intervals. The OCP transient is shown in Figure 20c. The initial potential at t = 1 s was −284.9 mV vs. SCE, and it gradually shifted in the anodic direction, reaching −209.7 mV vs. SCE at t = 3,600 s. The total potential shift over the 60-min monitoring period was 75.3 mV. The cathodic

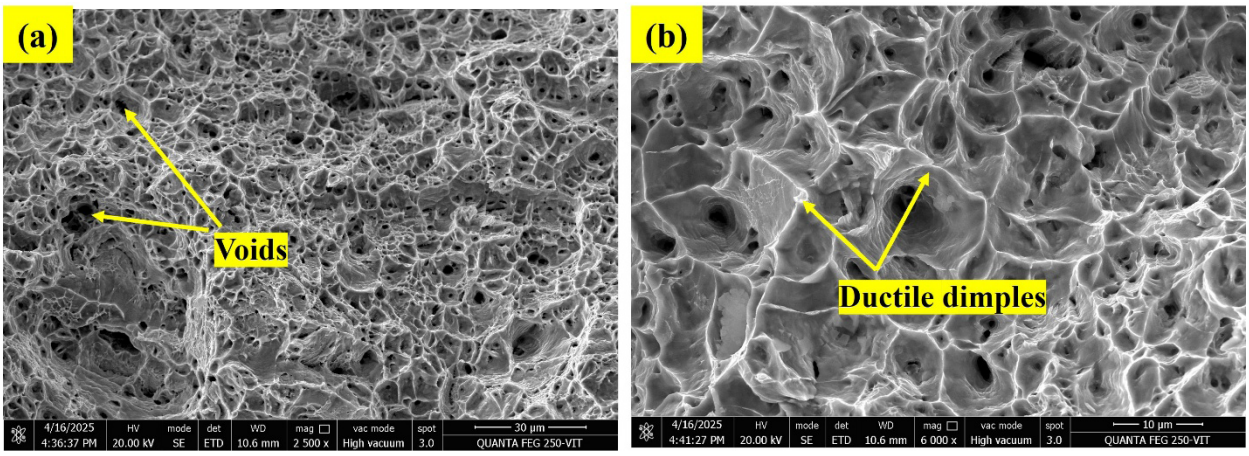

Figure 18. Fractographs of the bulk tensile specimen (0° orientation) of WAAM-fabricated HDSS at different magnifications: (a) Fracture surface with voids (scale bar: 30 μm), (b) ductile fracture surface showing ductile dimples (scale bar: 10 μm)
Abbreviations: HDSS: Hyper-duplex stainless steel; WAAM: Wire arc additive manufacturing.

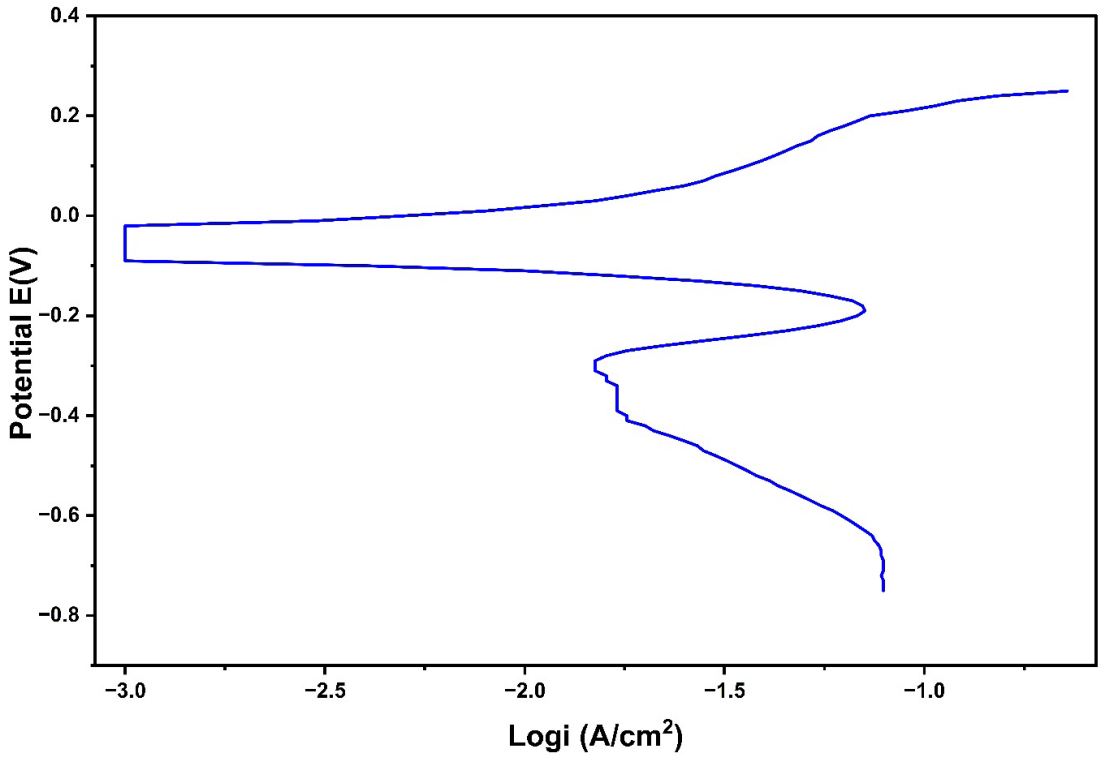

Figure 19. Potentiodynamic polarization curve (Tafel plot) for the WAAM-fabricated UNS S32707 HDSS sample measured in 3.5 wt.% NaCl solution
Abbreviations: HDSS: Hyper-duplex stainless steel; WAAM: Wire arc additive manufacturing.

drift of the OCP indicates progressive thickening and stabilization of the passive oxide film, as the increased film thickness shifts the mixed potential toward more negative values. During the final 300 s (last 5 min), the mean OCP was −214.9 ± 3.9 V (standard deviation < 3.9 mV), and the drift rate was 2.16 mV/min, confirming that the potential was approaching steady-state conditions. The final OCP value of −209.7 mV vs. SCE is consistent with the E_{corr}

obtained from the subsequent Tafel scan (E_{corr} = −0.0424 mV), with the difference attributable to the perturbation of the passive film during the polarization sweep.

Table 5. Potentiodynamic polarization data for the WAAM-fabricated HDSS sample in 3.5% NaCl solution (extracted from experimental Tafel scan)

Electrochemical parameters	Tafel data
Corrosion potential E_{corr} (V)	−0.0424
Corrosion current, I_{corr} (A)	7.222×10^{-6}
Corrosion current density, J_{corr} (A/cm²)	7.222×10^{-6}
Polarization resistance, Rp (Ω·cm²)	1.034×10^{4}
Anodic Tafel slope, β_a (V/dec)	0.229
Cathodic Tafel slope, β_c (V/dec)	0.689
Corrosion rate (mm/y)	0.07877

Abbreviations: HDSS: Hyper-duplex stainless steel; WAAM: Wire arc additive manufacturing.

3.11. Electrochemical impedance spectroscopy

Electrochemical impedance spectroscopy was performed at OCP on the WAAM-fabricated HDSS. The measured impedance data are presented as a Nyquist plot in Figure 20a, which shows the relationship between the real and imaginary impedance. To study the corrosion rate, oxide layer, and reaction parameters, EIS was conducted. The phase plot reveals the relationship between phase angle and frequency, whereas the Bode plot in Figure 20b shows the relationship between impedance magnitude and frequency. The Nyquist plot displays a partial capacitive arc in both Z' and |Z"|, which increased with decreasing frequency, characteristic of a charge-transfer-controlled process with the formation of a protective passive layer. The consistently negative *Z*" values across all measured frequencies confirm purely capacitive behavior, indicating that the passive film on the HDSS surface remains intact without evidence of inductive loops or film breakdown within the tested frequency range. The progressive increase in phase angle magnitude from −72.8° (100 Hz) to −168.7.0° (5,180 Hz) is consistent with an increasing capacitive contribution from the passive oxide film at lower frequencies. The resistance value of 14.7 Ω·cm² reflects the electrolyte resistance of the

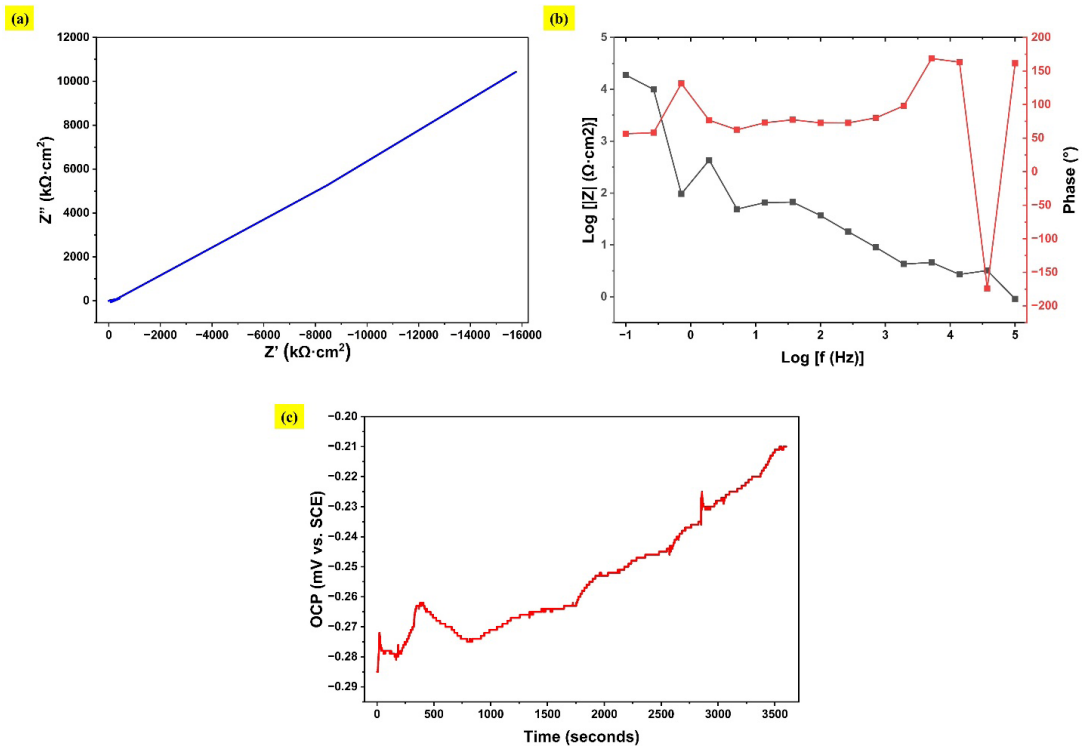

Figure 20. Electrochemical analysis of WAAM-fabricated UNS S32707 HDSS in 3.5 wt.% NaCl. (a) Nyquist plot showing impedance response over 0.1–100 kHz. (b) Bode impedance modulus vs. frequency. (c) OCP transient over 3,600 s showing anodic drift from −284.9 mV to −209.7 mV vs. SCE. Abbreviations: HDSS: Hyper-duplex stainless steel; OCP: Open-circuit potential; SCE: Saturated calomel electrode; WAAM: Wire arc additive manufacturing.

3.5 wt.% NaCl solution. Similar results were observed by Li *et al.*[53] during corrosion studies performed on HDSS 2707.

4. Conclusion

In this study, UNS S32707 HDSS was successfully fabricated via GMAW-based WAAM, targeting the subsea umbilical system and offshore components. The microstructural, mechanical, and electrochemical corrosion behavior were investigated. The significant findings are:

- A defect-free, 52-layer wall was successfully deposited with an inter-pass heat input of 0.2601 kJ/mm and an inter-pass temperature range of 110 °C–150 °C, as confirmed by X-ray radiography.
- EBSD analysis confirmed a well-balanced duplex microstructure consisting of 52.1% BCC ferrite and 47.4% FCC austenite, with a minor 0.5% σ phase confined to grain boundaries. No χ phase, Cr_2N, or γ_2 was observed, confirming the effective suppression of secondary phases through optimized interpass thermal temperature control.
- Ferrite exhibited a strong crystallographic texture, with inverse pole figure and pole figure intensities of 4.25 and 21.91 MUD, respectively. LAGB fractions were 92.63% in BCC and 63.44% in FCC, while the corresponding grain sizes were 54.8 μm and 14.7 μm, respectively.
- The WAAM-fabricated HDSS exhibited a UTS of 937 ± 7 MPa and a yield strength of 764 MPa. Consistent elongation values above 44% across all orientations confirmed the absence of embrittling phases.
- Potentiodynamic polarization test in 3.5 wt.% NaCl showed good corrosion resistance, with $E_{corr} = -0.0424$ V vs. SCE, $j_{corr} = 7.222 \times 10^{-6}$ A/cm^2, and a corrosion rate of 0.07877 mm/y.

Acknowledgments

The authors thank VIT University for supporting this research work.

Funding

The authors declare that no specific funding was received for this work.

Conflict of interest

The authors declare no conflict of interest.

Author contributions

Conceptualization: All authors
Data curation: Muppala Prardhan Yogya
Formal analysis: Muppala Prardhan Yogya
Investigation: Muppala Prardhan Yogya
Methodology: Muppala Prardhan Yogya
Project administration: Arivazhagan Natarajan
Resources: Arivazhagan Natarajan
Supervision: Arivazhagan Natarajan
Visualization: Muppala Prardhan Yogya
Writing–original draft: Muppala Prardhan Yogya
Writing–review & editing: Arivazhagan Natarajan

Ethics approval and consent to participate

Not applicable.

Consent for publication

Not applicable.

Availability of data

The data supporting the findings of this study are available from the corresponding author upon reasonable request.

References

1. Market Data Forecast. Duplex Stainless Steel Market Report. Accessed April 24, 2026. https://www.marketdataforecast.com/market-reports/duplex-stainless-steel-market
2. Dirisu P, Supriyo G, Martina F, Xu X, Williams S. Wire plus arc additive manufactured functional steel surfaces enhanced by rolling. *Int J Fatigue*. 2020;130:105237.

   doi: 10.1016/j.ijfatigue.2019.105237
3. Xiong J, Zhang G, Zhang W. Forming appearance analysis in multi-layer single-pass GMAW-based additive manufacturing. *Int J Adv Manuf Technol*. 2015;80(9-12):1767-1776.

   doi: 10.1007/s00170-015-7112-4
4. Kumar MDB, Bhasith AA, Kumar GSV, *et al*. Investigation of Microstructure and Mechanical Characteristics of Thin-walled Hastelloy C-276 Manufactured Through Pulsed-Arc Additive Manufacturing Technique. *Met Mater Int*. 2025;31(2):489-507.

   doi: 10.1007/s12540-024-01750-5
5. Ahn DG. Direct metal additive manufacturing processes and their sustainable applications for green technology: A review. *Int J Precis Eng Manuf Green Technol*. 2016;3(4):381-395.

   doi: 10.1007/s40684-016-0048-9
6. Bikas H, Stavropoulos P, Chryssolouris G. Additive manufacturing methods and modelling approaches: a critical review. *Int J Adv Manuf Technol*. 2016;83(1-4):389-405.

   doi: 10.1007/s00170-015-7576-2
7. Palmeira Belotti L, Van Dommelen JAW, Geers MGD, Goulas C, Ya W, Hoefnagels JPM. Microstructural characterisation

of thick-walled wire arc additively manufactured stainless steel. *J Mater Process Technol*. 2022;299:117373.

doi: 10.1016/j.jmatprotec.2021.117373

8. Haghdadi N, Laleh M, Moyle M, Primig S. Additive manufacturing of steels: a review of achievements and challenges. *J Mater Sci*. 2021;56(1):64-107.

doi: 10.1007/s10853-020-05109-0

9. Raj PN, Navaneethkrishnan PK, Sekar K, Joseph MA. Comparative study of mechanical, corrosion and erosion—corrosion properties of cast hyper-duplex and super-duplex stainless steels. *Int J Miner Metall Mater*. 2020;27(7):954-961.

doi: 10.1007/s12613-020-1984-5

10. Raha B. Study on Properties of Hyper-duplex Stainless Steel 7A of ASTM A-890 (CD3MWN). *Trans Indian Inst Met*. 2020;73(1):127-134.

doi: 10.1007/s12666-019-01811-z

11. Chail G, Kangas P. Super and hyper duplex stainless steels: structures, properties and applications. *Procedia Struct Integrity*. 2016;2:1755-1762.

doi: 10.1016/j.prostr.2016.06.221

12. Xiang H, Hu Y, Cao H, Liu D, Dong X. Erosion–corrosion behavior of SAF3207 hyper-duplex stainless steel. *Int J Miner Metall Mater*. 2019;26(11):1415-1426.

doi: 10.1007/s12613-019-1825-6

13. Göransson K, Nyman ML, Holmquist M, Gomes E. Sandvik SAF 2707 HD® (UNS S32707): a hyper-duplex stainless steel for severe chloride containing environments. *Rev Met Paris*. 2007;104(9):411-417.

doi: 10.1051/metal:2007207

14. Sun L, Sun Y, Lv C, *et al*. Studies on the degree of sensitization of hyper-duplex stainless steel 2707 at 900℃ using a modified DL-EPR test. *Corros Sci*. 2021;185:109432.

doi: 10.1016/j.corsci.2021.109432

15. Shang F, Wang Z, Chen X, Ji Z, Ren S, Qu X. UNS S32707 hyper-duplex stainless steel processed by powder injection molding and supersolidus liquid-phase sintering in nitrogen sintering atmosphere. *Vacuum*. 2021;184:109910.

doi: 10.1016/j.vacuum.2020.109910

16. Shang F, Chen X, Wang Z, *et al*. The Microstructure, Mechanical Properties, and Corrosion Resistance of UNS S32707 Hyper-Duplex Stainless Steel Processed by Selective Laser Melting. *Metals*. 2019;9(9):1012.

doi: 10.3390/met9091012

17. Ding J, Colegrove P, Mehnen J, *et al*. Thermo-mechanical analysis of Wire and Arc Additive Layer Manufacturing process on large multi-layer parts. *Comput Mater Sci*. 2011;50(12):3315-3322.

doi: 10.1016/j.commatsci.2011.06.023

18. Xu X, Ganguly S, Ding J, *et al*. Improving mechanical properties of wire plus arc additively manufactured maraging steel through plastic deformation enhanced aging response. *Mater Sci Eng A*. 2019;747:111-118.

doi: 10.1016/j.msea.2018.12.114

19. Zhang X, Zhou Q, Wang K, *et al*. Study on microstructure and tensile properties of high nitrogen Cr-Mn steel processed by CMT wire and arc additive manufacturing. *Mater Des*. 2019;166:107611.

doi: 10.1016/j.matdes.2019.107611

20. Das A, Yadav V, AlMangour B, *et al*. Additive manufacturing of graphene reinforced 316L stainless steel composites with tailored microstructure and mechanical properties. *Mater Chem Phys*. 2023;303:127826.

doi: 10.1016/j.matchemphys.2023.127826

21. Pan J, Wang J, Evernden M, Evans SI, Xu F. Experimental assessment of stiffening geometries for thin-walled structural steel plates made by wire arc additive manufacturing. *Results Eng*. 2026;29:108966.

doi: 10.1016/j.rineng.2026.108966

22. Wang J, Chen W, Meng H, Cui Y, Zhang C, Han P. Influence of sigma phase on corrosion and mechanical properties of 2707 hyper-duplex stainless steel aged for short periods. *J Iron Steel Res Int*. 2019;26(5):452-461.

doi: 10.1007/s42243-018-0175-3

23. Mukherjee T, Elmer JW, Wei HL, *et al*. Control of grain structure, phases, and defects in additive manufacturing of high-performance metallic components. *Prog Mater Sci*. 2023;138:101153.

doi: 10.1016/j.pmatsci.2023.101153

24. Kannan AR, Shanmugam NS, Rajkumar V, Vishnukumar M. Insight into the microstructural features and corrosion properties of wire arc additive manufactured super duplex stainless steel (ER2594). *Mater Lett*. 2020;270:127680.

doi: 10.1016/j.matlet.2020.127680

25. Queguineur A, Asadi R, Ostolaza M, *et al*. Wire arc additive manufacturing of thin and thick walls made of duplex stainless steel. *Int J Adv Manuf Technol*. 2023;127(1-2):381-400.

doi: 10.1007/s00170-023-11560-5

26. Kumar S, Krisam S, Jacob A, *et al*. Microstructures and element distributions in an aged hyper duplex stainless steel and corresponding hardness variation. *Mater Des*. 2020;194:108951.

doi: 10.1016/j.matdes.2020.108951

27. De Sampaio MTG, Furtado AB, Ignácio MDC, *et al*. Quantification of Deleterious Phase Precipitation in a Hyper

Duplex Stainless Steel Aged at 700-950 °C Using Optimized Linear Sweep Voltammetry: Effect of KOH Concentration. *J Mater Eng Perform*. 2025;34(13):12494-12507.

doi: 10.1007/s11665-024-10049-w

28. Yang R, Han S, Lei X, *et al*. Hot corrosion mechanism of laser metal deposited Ni-based single crystal superalloy under fuel gas atmosphere. *Surf Coat Technol*. 2023;474:130057.

doi: 10.1016/j.surfcoat.2023.130057

29. Schuster R, Keplinger A, Jacob A, *et al*. In-situ XRD investigation of σ phase precipitation kinetics during isothermal holding in a hyper duplex stainless steel. *Mater Charact*. 2023;203:113124.

doi: 10.1016/j.matchar.2023.113124

30. Wang H, Wang A, Li C, Yu X, Xie J, Liu C. Effect of Secondary-Phase Precipitation on Mechanical Properties and Corrosion Resistance of 00Cr27Ni7Mo5N Hyper-Duplex Stainless Steel during Solution Treatment. *Materials*. 2022;15(21):7533.

doi: 10.3390/ma15217533

31. Wang Y, Sukenaga S, Shibata H, Wang Q, Mu W. Combination of In Situ Confocal Microscopy and Calorimetry to Investigate Solidification of Super- and Hyper-Duplex Stainless Steels. *Steel Res Int*. 2023;94(11):2200960.

doi: 10.1002/srin.202200960

32. Zhang Y, Wu S, Cheng F. A specially-designed super duplex stainless steel with balanced ferrite:austenite ratio fabricated via flux-cored wire arc additive manufacturing: Microstructure evolution, mechanical properties and corrosion resistance. *Mater Sci Eng A*. 2022;854:143809.

doi: 10.1016/j.msea.2022.143809

33. Eriksson M, Lervåg M, Sørensen C, *et al*. Additive manufacture of superduplex stainless steel using WAAM. In: Pantelakis S, Koubias S, eds. *MATEC Web Conf*. 2018;188:03014.

doi: 10.1051/matecconf/201818803014

34. Wittig B, Zinke M, Jüttner S. Influence of arc energy and filler metal composition on the microstructure in wire arc additive manufacturing of duplex stainless steels. *Weld World*. 2021;65(1):47-56.

doi: 10.1007/s40194-020-00995-z

35. Nikam PP, Arun D, Ramkumar KD, Sivashanmugam N. Microstructure characterization and tensile properties of CMT-based wire plus arc additive manufactured ER2594. *Mater Charact*. 2020;169:110671.

doi: 10.1016/j.matchar.2020.110671

36. Hengsbach F, Koppa P, Duschik K, *et al*. Duplex stainless steel fabricated by selective laser melting - Microstructural and mechanical properties. *Mater Des*. 2017;133:136-142.

doi: 10.1016/j.matdes.2017.07.046

37. Chen MT, Chen Y, Zuo W, *et al*. Experimental investigation on the tensile behavior of wire arc additively manufactured duplex stainless steel plates. *Eng Struct*. 2024;321:118764.

doi: 10.1016/j.engstruct.2024.118764

38. Kannan AR, Shanmugam NS, Ramkumar KD, Rajkumar V. Studies on Super Duplex Stainless Steel Manufactured by Wire Arc Additive Manufacturing. *Trans Indian Inst Met*. 2021;74(7):1673-1681.

doi: 10.1007/s12666-021-02257-y

39. Zhang X, Wang K, Zhou Q, *et al*. Microstructure and mechanical properties of TOP-TIG-wire and arc additive manufactured super duplex stainless steel (ER2594). *Mater Sci Eng A*. 2019;762:138097.

doi: 10.1016/j.msea.2019.138097

40. Chiniforoush EA, Gholizadeh T, Jandaghi MR, Moverare J, Gür CH. Impact of active to inert shielding gas transition on the corrosion behavior of wire arc additively manufactured duplex stainless steel. *Mater Des*. 2025;253:113907.

doi: 10.1016/j.matdes.2025.113907

41. Keplinger A, Martinez C, Hausbauer M, Kapp M. Early Stages of Deleterious Phases in Super and Hyper Duplex Stainless Steel and Their Effect on Toughness. *Berg Huettenmaenn Monatsh*. 2020;165(1):33-39.

doi: 10.1007/s00501-019-00936-4

42. Akbarzadeh E, Yurtışık K, Hakan Gür C, Saeid T, Tavangar R. Influence of Shielding Gas on the Microstructure and Mechanical Properties of Duplex Stainless Steel in Wire Arc Additive Manufacturing. *Met Mater Int*. 2024;30(7):1977-1996.

doi: 10.1007/s12540-023-01623-3

43. Haghdadi N, Cizek P, Hodgson PD, Tari V, Rohrer GS, Beladi H. Effect of ferrite-to-austenite phase transformation path on the interface crystallographic character distributions in a duplex stainless steel. *Acta Mater*. 2018;145:196-209.

doi: 10.1016/j.actamat.2017.11.057

44. He XY, Xu ZP, Rohrer GS, Kong C, Primig S, Haghdadi N. Three-dimensional analysis of the delta-ferrite to austenite phase transformation in an additively manufactured duplex stainless steel. *Mater Charact*. 2025;221:114745.

doi: 10.1016/j.matchar.2025.114745

45. Biradar NS, Raman R. Grain Refinement in Al-Mg-Si Alloy TIG Welds Using Transverse Mechanical Arc Oscillation. *J Mater Eng Perform*. 2012;21(11):2495-2502.

doi: 10.1007/s11665-012-0207-2

46. Eghlimi A, Shamanian M, Eskandarian M, Zabolian A, Szpunar JA. Characterization of microstructure and texture across dissimilar super duplex/austenitic stainless steel

weldment joint by austenitic filler metal. *Mater Charact*. 2015;106:208-217.

doi: 10.1016/j.matchar.2015.05.036

47. Abe M, Hiura A, Ishida K, Nishizawa T. Grain Growth in Duplex Stainless Steels. *Tetsu-to-Hagane*. 1984;70(15):2025-2032.

doi: 10.2355/tetsutohagane1955.70.15_2025

48. Chiniforoush EA, Gholizadeh T, Jandaghi MR, Moverare J, Gür CH. Investigation of travel speed effects on microstructure and corrosion behavior of duplex stainless steel in wire-based DED additive manufacturing. *J Mater Res Technol*. 2025;37:1486-1504.

doi: 10.1016/j.jmrt.2025.06.143

49. Krupp U, Söker M, Giertler A, *et al*. The potential of spinodal ferrite decomposition for increasing the very high cycle fatigue strength of duplex stainless steel. *Int J Fatigue*. 2016;93:363-371.

doi: 10.1016/j.ijfatigue.2016.05.012

50. Van Ede MC, Angst U. Tafel slopes and exchange current densities of oxygen reduction and hydrogen evolution on steel. *Corros Eng Sci Technol*. 2024;59(1):39-55.

doi: 10.1177/1478422X241227829

51. Murmu M, Saha SKr, Murmu NC, Banerjee P. Amine cured double Schiff base epoxy as efficient anticorrosive coating materials for protection of mild steel in 3.5% NaCl medium. *J Mol Liq*. 2019;278:521-535.

doi: 10.1016/j.molliq.2019.01.066

52. Cai S, Lu K, Li X, Wen L, Huang F, Jin Y. Quantitative micro-electrochemical study of duplex stainless steel 2205 in 3.5wt% NaCl solution. *Int J Miner Metall Mater*. 2022;29(11):2053-2063.

doi: 10.1007/s12613-021-2291-5

53. Li H, Zhou E, Zhang D, *et al*. Microbiologically Influenced Corrosion of 2707 Hyper-Duplex Stainless Steel by Marine Pseudomonas aeruginosa Biofilm. *Sci Rep*. 2016;6(1):20190.

doi: 10.1038/srep20190